รายงานวิจัยฉบับสมบูรณ์

ผลของอุณหภูมิการเผาที่มีต่อการก่อเกิดเฟส โครงสร้างจุลภาค และสมบัติไดอิเล็กทริกของเซรามิก $Bi_{0.5}(Na_{0.74}K_{0.16}Li_{0.10})_{0.5}TiO_3$ ที่สังเคราะห์ด้วยวิธีการเผาไหม้

The effect of firing temperatures on phase formation, microstructure and dielectric properties of $Bi_{0.5}(Na_{0.74}K_{0.16}Li_{0.10})_{0.5}TiO_3$ ceramics synthesized via the combustion route

ผศ.ดร.ธีระชัย บงการณ์

กันยายน 2559

สัญญาเลขที่ R2559C053

รายงานวิจัยฉบับสมบูรณ์

ผลของอุณหภูมิการเผาที่มีต่อการก่อเกิดเฟส โครงสร้างจุลภาค และสมบัติไดอิเล็กทริกของเซรามิก $Bi_{0.5}(Na_{0.74}K_{0.16}Li_{0.10})_{0.5}TiO_3$ ที่สังเคราะห์ด้วยวิธีการเผาไหม้

The effect of firing temperatures on phase formation, microstructure and dielectric properties of $Bi_{0.5}(Na_{0.74}K_{0.16}Li_{0.10})_{0.5}TiO_3$ ceramics synthesized via the combustion route

ผศ.ดร.ธีระชัย บงการณ์
ภาควิชาฟิสิกส์ คณะวิทยาศาสตร์ มหาวิทยาลัยนเรศวร

สนับสนุนโดยกองทุนวิจัยมหาวิทยาลัยนเรศวร

กิตติกรรมประกาศ

งานวิจัยนี้ได้รับการสนับสนุนงบประมาณจากกองทุนวิจัยมหาวิทยาลัยนเรศวร ผู้วิจัยและคณะขอขอบพระคุณ ณ โอกาสนี้

ขอขอบคุณเจ้าหน้าที่ภาควิชาฟิสิกส์ คณะวิทยาศาสตร์ มหาวิทยาลัยนเรศวร ทุกท่านซึ่งอำนวยความสะดวกเกี่ยวกับอุปกรณ์เครื่องมือต่างๆ

ขอขอบคุณ Science Lab Center คณะวิทยาศาสตร์ มหาวิทยาลัยนเรศวร ที่สนับสนุนเครื่องมือและอุปกรณ์ในการทำวิจัย

ผศ.ดร.ธีระชัย บงการณ์

หัวข้อวิจัย ผลของอุณหภูมิการเผาที่มีต่อการก่อเกิดเฟส โครงสร้างจุลภาค และสมบัติไดอิเล็กทริกของเซรามิก $Bi_{0.5}(Na_{0.74}K_{0.16}Li_{0.10})_{0.5}TiO_3$ ที่สังเคราะห์ด้วยวิธีการเผาไหม้

นักวิจัย ผศ.ดร.ธีระชัย บงการณ์

บทคัดย่อ

งานวิจัยนี้เป็นการศึกษาการก่อเกิดเฟส โครงสร้างจุลภาค และสมบัติทางไฟฟ้าของเซรามิก BZT และ BNT สังเคราะห์โดยวิธีเผาไหม้ โดยมุ่งเน้นศึกษาอุณหภูมิการเผาที่มีผลต่อการก่อเกิดเฟส โครงสร้างจุลภาคและสมบัติไดอิเล็กทริกของเซรามิก $Bi_{0.5}(Na_{0.74}K_{0.16}Li_{0.10})_{0.5}TiO_3$ หรือ BNKL1610 ผลของอุณหภูมิการเผาที่สูงก่อให้เกิดเฟสแปลกปลอมบนผงผลึกและเซรามิก BNKLT1610 การระเหยของสารตั้งต้นและผลิตภัณฑ์เป็นเหตุทำให้เกิดเฟสแปลกปลอมระหว่างการเผาแคลไซน์และซินเตอร์ รูปแบบการเลี้ยวเบนรังสีเอกซ์ของเซรามิก BNKLT1610 แสดงเฟสร่วมระหว่างเฟสรอมโบฮีดรอลและเททระโกนอล แต่ละเฟสสัมพันธ์กับอุณหภูมิการเผาซินเตอร์ ค่าไดอิเล็กทริก ณ T_d ถูกแสดงในทุกตัวอย่าง ในขณะที่ค่าไดอิเล็กทริกสูงสุด T_m ถูกพบเพียงตัวอย่างที่เผาซินเตอร์ที่อุณหภูมิสูง ผลของไดอิเล็กทริกส่งผลให้เกิดโครงสร้างลักษณะคอเซลล์สำหรับตัวอย่างที่เตรียม การเพิ่มอุณหภูมิซินเตอร์ทำให้เกรนคอร์ มีขนาดเพิ่มขึ้นและเกรนเซลล์มีขนาดแคบลง ค่าไดอิเล็กทริกสูงสุด ε_r เท่ากับ 1,210 พบที่ตัวอย่างเผาซินเตอร์ที่อุณหภูมิ 1,000 °C ซึ่งสูงกว่า BNKLT1610 ที่เตรียมโดยวิธีปฏิกิริยาสถานะของแข็ง

Research Topic: The effect of firing temperatures on phase formation, microstructure and dielectric properties of $Bi_{0.5}(Na_{0.74}K_{0.16}Li_{0.10})_{0.5}TiO_3$ ceramics synthesized via the combustion route

Researcher: Assist.Prof.Dr.Theerachai Bongkarn

ABSTRACT

This work constitutes a major study of phase formation, microstructure and electrical properties of BZT and BNT-based ceramics which were synthesized through the combustion route. the study is focused on the effects of firing temperature on phase formation, microstructure and the dielectric properties of $Bi_{0.5}(Na_{0.74}K_{0.16}Li_{0.10})_{0.5}TiO_3$ or BNKL1610 ceramics synthesized via the combustion route. The results demonstrated that firing temperature highly influences the secondary phase formed on BNKLT1610 powders and ceramics. The vaporization of raw materials and products caused the formation of a secondary in calcined powders and sintered ceramics, respectively. The XRD patterns suggested the BNKLT1610 ceramics show the coexistence of rhombohedral and tetragonal phases and the relative amount of each phase correlates with the sintering temperature. The dielectric peak at depolarization temperature (T_d) was exhibited in all samples while the dielectric peak at maximum dielectric temperature (T_m) was observed only the samples sintered at high temperatures. The dielectric results persuade core-shell structure is formed in prepared samples. Increasing sintering temperature caused the grain core to enlarger and the grain shell to become thinner. The dielectric constants are highly affected by secondary phase formation and densification. The highest value ε_r of 1,210 was obtained from the sample sintered at 1,000 °C, which is significantly higher than BNKLT1610 prepared via the solid-state reaction method.

CHARPTER I

INTRODUCTION

Rational for the study

Lead-free piezoelectric ceramics have attracted increasing attention because the PbO in lead piezoelectric ceramics is volatile and detrimental to human health and the environment. Bismuth sodium titanate ($(Bi_{0.5}Na_{0.5})TiO_3$, BNT), discovered by Smolensky, et al. in 1960 [1], is one of the most important lead-free piezoelectric materials. This ceramic shows strong ferroelectricity of P_r = 38 μC/cm^2 and high Curie point of T_c= 540 °C [2]. However, because of its high coercive field (E_c = 73 kV/mm) and relatively large conductivity, pure BNT is difficult to be poled and is limited in its typical applications [3]. This is because both Bi and Na at the A-site of ABO_3 perovskite tend to evaporate during sintering at high temperature. Therefore, A-site vacancies should be easily formed in BNT ceramics and effect the conductivity of the materials [4].

Many researchers have attempted to improve BNT-properties by selecting some cation substituted on the A- site of a BNT system [5, 6, 7, 8, 9, 10]. Yang, et al. [5] studied the effects of K substituted to Na at the A-site of BNT perovskite in a range of 10-20 mol% on crystal structure, microstructure and electrical properties. The results indicated 18 mol% of K substitution induced an occurrence in the MPB region between the rhombohedral-tetragonal phases, which enhanced the dielectric properties of the ceramics. Lin, et al. [10] demonstrated that a small amount of Li could decrease sintering temperature and improve the densification of BNT-BT ceramics. The study on Li and K substituted BNT was extensively investigated by Lu, et al. [2]. The XRD results indicated that the $Bi_{0.5}(Na_{0.74}K_{0.16}Li_{0.10})_{0.5}TiO_3$ or BNKL1610 composition showed the coexistence of a rhombohedral and tetragonal structure which suggests this composition is located near the MPB region. Moreover, the substitution of Li and K for BNKL1610 greatly improved the electrical properties of BNT such as increasing d_{33} from 78 to 160 pC/N, increasing k_p from 0.16 to 0.35 and increasing ε_r from 420 to 1080.

In terms of the preparation process, BNT-based ceramics were fabricated via the solid-state reaction method [11, 12]. The raw materials were heat treated at 800-900 °C for 2-5 h in a calcination process and at 1,050-1,200 °C for 2-5 h in sintering process [11, 12]. The secondary phases were formed due to the vaporization of raw materials at high temperature in the preparation processes [11]. To avoid this problem, BNT and BNT-based ceramics have been prepared by several wet chemical methods such as the sol-gel route [13], the hydrothermal method [14] and the molten salt synthesis [15]. However, it is well known that these chemical methods require a long processing time, special equipment and have a complex procedure [17].

Recently, the combustion technique has become an attractive technique to prepare ferroelectric materials because it's uncomplicated [16, 17, 18, 19]. Moreover, the released energy from fuel decomposition helps to reduce the firing temperatures in the preparation process. Therefore, the purpose of this study was to synthesize BNKLT1610 ceramics via the combustion route. The effects of firing temperatures on phase formation, microstructure and dielectric properties of BNKLT1610 ceramics were also investigated.

Objectives of the study

To study the effects of firing temperature on phase formation, microstructure and dielectric properties of BNKLT1610 ceramics synthesized through the combustion technique.

Expected outputs of the study

To understand the effects of firing temperature on phase formation, microstructure and dielectric properties of the BNKLT1610 ceramics synthesized via the combustion technique.

CHARPTER II

RELATED THEORICAL

Piezoelectricity

The word "piezoelectricity" is translated from the Greek word *piezein* which means pressure electricity. This word was discovered by Jacques Curie and Pierre Curie in 1880 [20]. Piezoelectricity is an electromechanical coupling phenomenon occurring in non-centrosymmetric crystalline materials. A piezoelectric crystal will develop an electrical charge in response to an applied mechanical stress to materials (direct effect). Conversely electrical energy can be converted into mechanical energy through the reorientation of dipoles, which rearranges the crystal lattice (converse effect). The piezoelectric effect is linear (first order), producing a strain proportional to the electric field with the displacement directionally dependent on the sign of the applied electric field. The schematic diagram of direct effect and converse effect is illustrated in Figure 1.

Electrostriction is a quadratic (second order) effect in which strain is independent of direction and proportional to the square of the electric field. This phenomenon is the electromechanical response observed in a centrosymmetric crystal, for which no polar properties exist. The elctrostrictive effect is usually very weak with strain on the order of 10^{-11} in simple oxides and 10^{-6} in perovskite oxide. However, some perovskites with high dielectric constants (indicating a high degree of polarizability) can exhibit large electrostrictive electromechanical coupling, with strains on the order of 10^{-3}. High-strain electrostrictors are the preferred materials for high precision controller actuator applications, for they have negligible hysteresis (i.e. no shift of the initial zero position) and do not require electric polling to preferentially orient dipoles or domains [21].

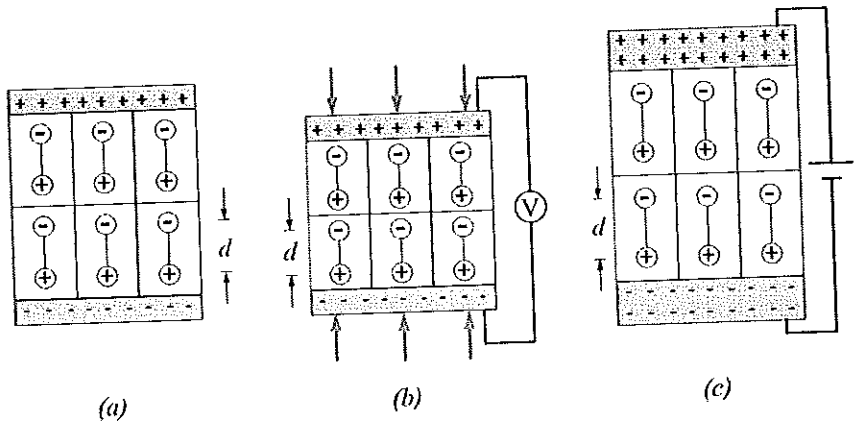

Figure 1 (a) Schematic illustration of electric dipoles within piezoelectric materials, (b) Compressive stresses on materials cause a voltage difference (direct effect), (c) Applied voltage causes materials deform thecrystal lattice (converse effect) [21]

Ferroelectricity

Ferroelectricity (FE) was first discovered in Rochelle salt in 1921. At that time, it was called Seignette-electricity, honoring its discoverer. For the past few decades, ferroelectric materials have received great interest because of their various uses for many applications such as high-permittivity capacitors, pyroelectric sensors, piezoelectric transducers, eletrooptic devices and PTC thermistors [22].

A crystal is ferroelectric when it possesses at least two equilibrium orientations of the spontaneous polarization in the absence of an external electric field. Its spontaneous polarization can be switched between those orientations by an applied electric field. The polar character of the orientation states should represent an absolutely stable configuration in a null field [22]. Among the 32 crystal classes, eleven of them are characterized by the existence of a center of symmetry. The remaining 21 crystal classes do not have a center of symmetry. Thus, it is possible for the 21 groups to (i) have one or more polar axes, and (ii) possess odd-rank tensor properties. The only exception is the group 432. Although it lacks a center of symmetry, it has other symmetry operations that destroy polarity. All non-centrosymmetric point groups exhibit a piezoelectric effect that is defined by a change of electric polarity under applied stress. Out of the twenty piezoelectric classes, ten

possess a unique polar axis. The spontaneous polarization depends on temperature. This is called the pyroelectric effect. Ferroelectric crystals belong the pyroelectric family, which in addition has a spontaneous polarization which can be reversed by an external electric field. Among all ferroelectric materials, the most extensively studied and widely used are the perovskite crystal. A perfect perovskite structure has a general formula of ABO_3, where A represents a divalent or trivalent cation, and B is typically a tetravalent or trivalent cation. The interrelationship of piezoelectric and subgroup on the basis of symmetry is showed in Figure 2.

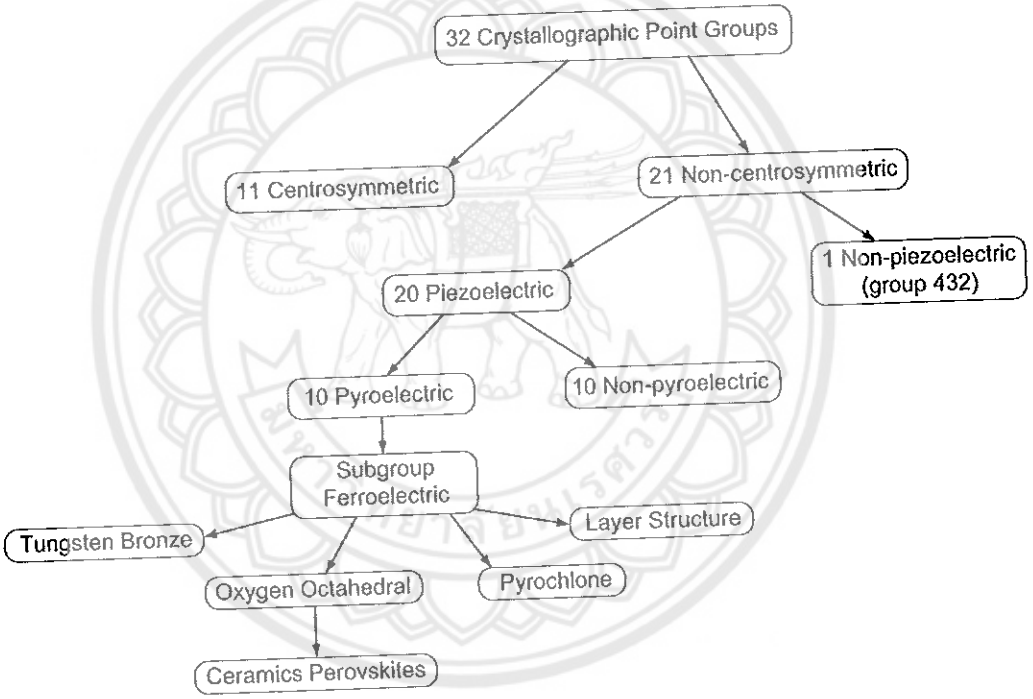

Figure 2 Interrelationship of piezoelectric and subgroup on the basis of symmetry

The origin of ferroelectricity in this family of materials can be explained by the well-known example of barium titanate ($BaTiO_3$). As shown in Figure 3, the Ba^{2+} and Ti^{4+} cations are located at A-site and B-site of the unit cell, respectively [20].

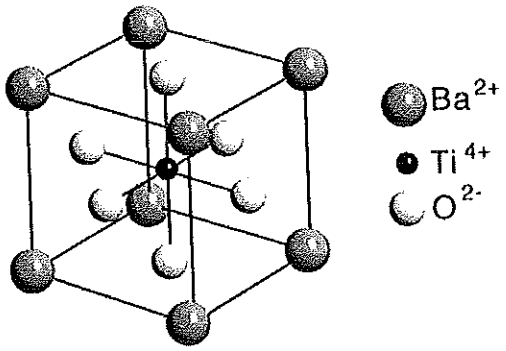

Figure 3 Ion positions in $BaTiO_3$

Typical interested properties of ferroelectric ceramics materials

1. Dielectric properties

Consider two metal parallel plates of area A separated by a distance d in vacuum (Figure 4(a)). Attaching these plates to a simple electric circuit and closing the circuit will result in a transient surge of current that rapidly decays to zero. As shown in Figure 4(b). Given that

$$Q = \int I \, dt \qquad \text{[Eq.1]}$$

The area under the I versus t curve is the total charge that has passed through the circuit and is now stored on the parallel plates.

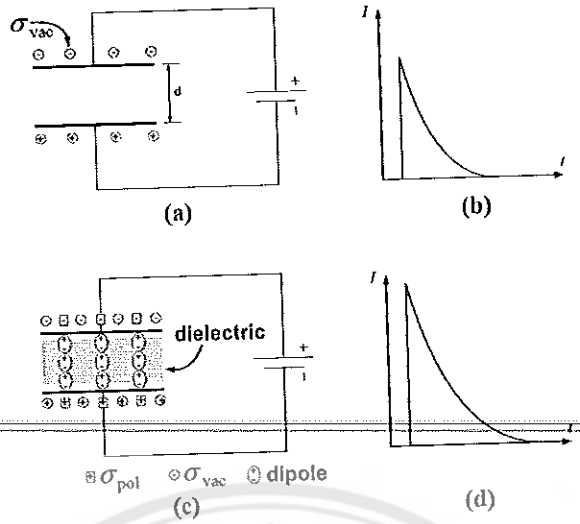

Figure 4 (a) Parallel-plate capacitor of area A and separation d in vacuum attached to a voltage source, (b) Closing of the circuit causes a transient surge of current to flow through the circuit, (c) Parallel-plate capacitor of area A and separation dielectric materials is placed between the plates, (d) Closing of the circuit results in a charge stored on the parallel plates of (c) circuit

Repeating the experiment at different voltages V and plotting Q versus V should yield a straight line (as shown in Figure 5). The well known relationship is

$$Q = CV \qquad \text{[Eq.2]}$$

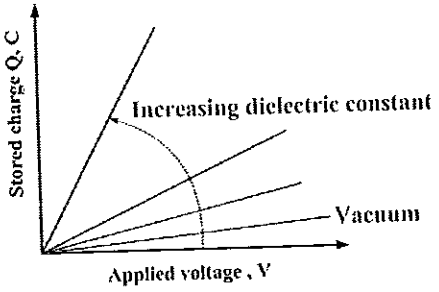

Figure 5 Functional dependence of Q on applied voltage. Slope of curve is related to the dielectric constant of the material

The slope of the Q versus V curve is the capacitance C_{vac} of the parallel plates in vacuum, given by

$$C_{\text{vac}} = \frac{\varepsilon_0 A}{d} \qquad \text{[Eq.3]}$$

Where ε_0 is the permittivity of free space, which is a constant equal to $8.85 \times 10^{-12} \text{C}^2/(\text{J} \cdot \text{m})$.

If a dielectric which can be a gas, liquid or solid is introduced between the plates of the capacitor (Figure 4(c)), the current that flows through the external circuit and is stored on the capacitor plates will increase (Figure 4(d)). Repeating the experiment at different voltages and plotting the total charge stored on the capacitor versus the voltage applied will again result in a straight line but with a larger slope than that for vacuum (Figure 5). The capacitance of the parallel plates is modified to form

$$C = \frac{\varepsilon A}{d} \qquad \text{[Eq.4]}$$

Where ε is the dielectric constant of the material between the parallel plates. The relative permittivity or dielectric constant of a material ε_r is defined as

$$\varepsilon_r = \frac{\varepsilon}{\varepsilon_0} \qquad \text{[Eq.5]}$$

Which when combined with Eq.4 and Eq.5 gives

$$C = \frac{\varepsilon_r \varepsilon_0 A}{d} = \varepsilon_r C_{\text{vac}} \qquad \text{[Eq.6]}$$

Thus ε_r is a dimensionless parameter that compares the charge-storing capacity of a material to that of vacuum.

2. Polarization

By combining of the Eq.2 and Eq.3, the σ_{vac} is the surface charge in vacuum and defined as

$$\sigma_{\text{vac}} = \left[\frac{Q}{A}\right]_{\text{vac}} = \frac{\varepsilon_0 V}{d} = \varepsilon_0 E \qquad \text{[Eq.7]}$$

When a dielectric is introduced between the parallel plates (Figure 4(c)), the surface charge on the parallel plates increases to

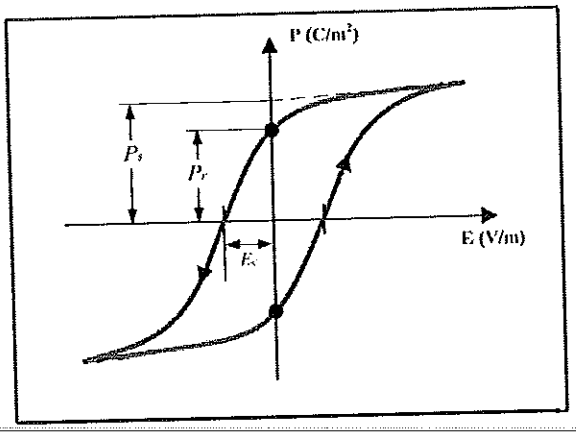

Figure 6 A typical ferroelectric hysteresis loops

4. Phase transition and Curie temperature

All ferroelectric materials have a transition temperature called the Curie temperature (T_c) [23]. At a temperature $T > T_c$ the crystal does not exhibit ferroelectricity. While $T < T_c$, the crystal shows ferroelectric characteristics. On decreasing the temperature through the Curie point, a ferroelectric crystal undergoes a phase transition from a non-ferroelectric phase to a ferroelectric phase. If there are more than one ferroelectric phases, the temperature at which the crystal transforms from one ferroelectric phase to another is called the transition temperature.

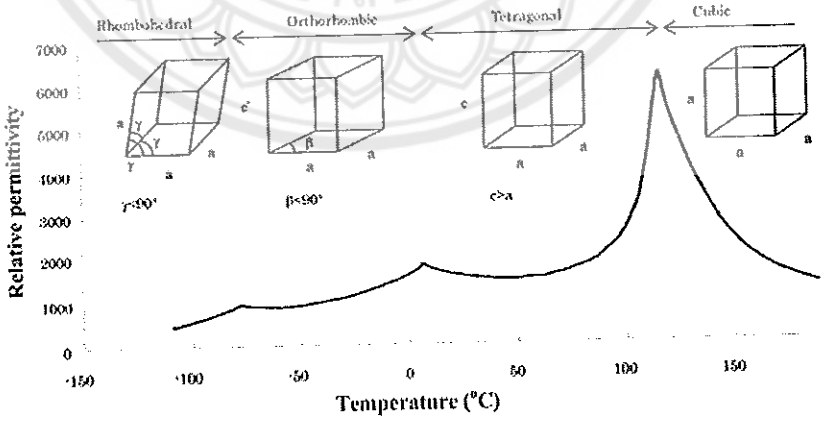

Figure 7 Variation of relative permittivity with temperature for $BaTiO_3$ [20]

Figure 7 shows the variation of the relative permittivity with temperature of $BaTiO_3$. The crystal is cooled from its paraelectric cubic phase to the ferroelectric

tetragonal, orthorhombic, and rhombohedral phases, respectively. Near the Curie temperature or phase transition temperatures, thermodynamic properties including dielectric, elastic, optical, and thermal constants show an anomalous behavior. This is due to a distortion in the crystal as the phase structure changes. The temperature dependence of the dielectric constant above the Curie point ($T > T_c$) in ferroelectric crystals is performed by the Curie-Weiss law:

$$\varepsilon_r = \frac{A}{T - \theta_c} \qquad \text{[Eq.12]}$$

Where A is a constant for a given material and θ_c is a temperature near to but not identical with the Curie temperature [20].

Typical ferroelectric matrials: Barium titanate (BT)

At high temperature, barium titanate ($BaTiO_3$) is cubic structure with the ion arranged as in Figure 8(a). Below the Curie point (approximately 120°C), the structure is slightly distored to tetragonal with the *c/a* ratio of around 1.01 and is stable. The spontaneous polarization is along one of the (001) directions in the original cubic structure. Between 0°C and -90°C, the ferroelectric orthorhombic phase is stable with the polarization along one of the (110) directions in the original cubic structure. When decreasing the temperature below -90°C the phase transition from the orthorhombic to ferroelectric rhombohedral phase leads to polarization along one of the [111] cubic directions. The phase transition behavior of $BaTiO_3$ is illustrated in Figure 7.

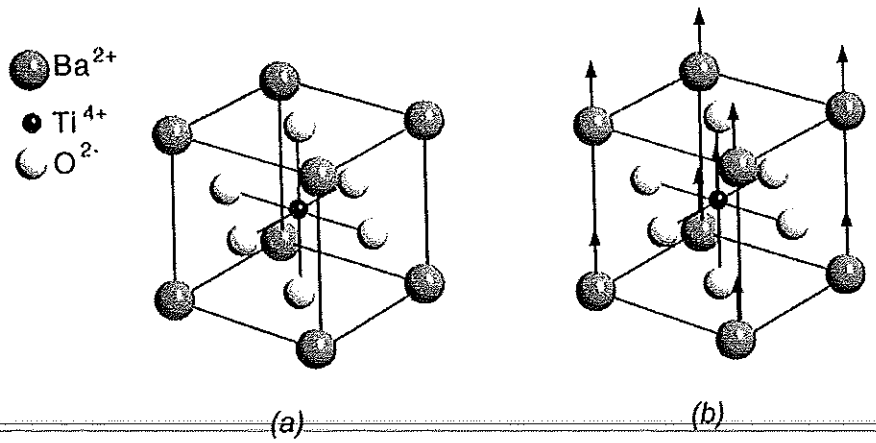

Figure 8 The crystal structures of BaTiO3 (a) Above Curie point show cubic structure, (b) Below Curie point the structure is tetragonal form with Ba^{2+} and Ti^{4+}slightly shifted relative to O^{2-}

The spontaneous polarization on cooling $BaTiO_3$ below the Curie point is due to changes in the crystal structure. As shown in Figure 8(b). Below Curie point, the structure of $BaTiO_3$ changes from a cubic to a tetragonal phase. The center of positive charges (Ba^{2+} and Ti^{4+} ions) is slightly shifted relative to negative charges (O^{2-} ion) which leads to the formation of electric dipoles. The spontaneous polarization developed is the net dipole moment produced per unit volume for the dipoles pointing in a given direction.

Typical preparation technique for ferroelectric ceramics

Solid state reaction method

The first step in the conventional method for preparing ferroelectric ceramics based on the solid state reaction method is weighing the starting materials according to the stoichiometric composition. After mixing and grinding, the mixture is usually calcined to produce the desired compound by combination reaction. Synthesis reaction of a compound is caused from the chemical reaction of raw materials, which occurs by atomic diffusion among particles at temperatures below the melting point of these raw materials. Using the diffusion laws, an equation describing the speed of solid phase reaction can be derived;

$$\left(1-(1-x)^{1/3}\right)^2 = \frac{2D't}{r^2} = 2Dt \qquad \text{[Eq.13]}$$

with

$$D = C\exp\left(\frac{-Q}{RT}\right) \qquad \text{[Eq.14]}$$

Where C is a constant related to the radius r of the particle, R is the gas constant, T is the absolute temperature and Q is the activation energy. This equation shows that the volume ratio x of the product increases with the increase of reaction temperatures T and reaction time t.

After calcination, the calcined powders are pressed in the mold and sintered at a higher temperature than that of the calcination. The ceramic products are densified after sintering and the grain size of the ceramic increases with increased sintering temperature.

Sol-gel method

The sol-gel process uses inorganic or metal-organic as precursors [10]. In aqueous or organic solvents, the precursors are hydrolyzed and condensed to form inorganic polymers composed of M-O-M bonds. In case of inorganic precursors, hydrolysis proceeds by the removal of a proton from an aqua ion to form a hydroxo (-OH) or oxo (=O) ligand. Condensation reactions involving the hydroxo ligands result in the formation of bridging hydroxyl (M-p(OH)-M) or oxo (M-O-M) bonds. Normally, monomeric aqueous ions are only stable at low pH and various monomeric or oligomeric anions are observed at high pH. At intermediate pH, well-defined polynuclear ions are often a stable solution. The the metal solubility is normally limited there. When it is exceeded, it results in the precipitation of oxyhydroxides or oxides.

Co-precipitation method

The concept of the co-precipitation technique is to transfer impurities to a precipitate concurrently with the deposition of some primary substances. Co-precipitation proceeds in two stages. In the first stage, the impurity is trapped either on the surface or inside the growing particles. If the growing particles have a crystal structure, then the impurity will become localized at regions of the solid phase with a perfect structure. During rapid precipitation, the growing particles will trap non-

equilibrium impurities, which are usually inhomogeneously distributed through the volume of the solid phase. In the second stage, the concentration of defects within the precipitate decreases and the particles are flocculated. Impurities trapped during the first stage return either partially or completely to the medium. The concentration of impurities in the solid phase becomes equalized. The crystals acquire an equilibrium composition that depends only on the composition and temperature of the medium.

Hydrothermal synthesis method

Hydrothermal synthesis is the crystallizing of substances from high-temperature aqueous solutions at high vapor pressures. Hydrothermal synthesis can be defined as a method of synthesizing single crystals which depends upon the solubility of minerals in hot water under high pressure. The crystal growth is formed in an apparatus consisting of a steel pressure vessel. A gradient of temperature is maintained at the opposite ends of the growth chamber. The hotter end dissolves the nutrient and the cooler end causes seeds to take on additional growth.

Combustion technique

The combustion synthesis method is modified from the solid state reaction method. It is an attractive method for preparing electroceramic materials, which involves a self-sustained reaction between reaction materials and fuel (e.g., urea, glycine, citric acid). The reaction converts the initial mixture typically to a fine well-crystalline powder of desired composition [20, 21, 22]. The combustion reaction gives out the energy that can be effectively applied to the raw materials. The released energy speeds up the chemical reaction of the raw materials and also decreases the reaction temperature. Moreover, the combustion technique is simple, inexpensive and less time consuming in comparison with other methods.

Sintering process

After the powders are synthesized, the pellets should heat at high temperature to produce the desired microstructure. This stage is called in term sintering. The process of sintering consists of three stages: an initial, intermediate, and final stage [24]. For an initial stage, the green body has a low density and lacking in physical integrity. There is a small degree of adhesion between adjacent particles. After heat treatment, the local point of contact initially joins without shrinkage. This is

accompanied by a smoothing of the free surface of the particles. After that, the neck formation at the contact point occurs (Figure 9). If the relative green density after the forming of the particle was 60%, the density after the initial stage would be about 70% of the theoretical density.

In an intermediate state, the significant results are the neck growth, pores forming arrays of interconnected channels and particle centers approaching one another. The high curvatures exhibited in the initial stage are assumed to have been eliminated. Densification is assumed to occur by the pore simply shrinking to reduce their radius. This stage is considered to have a relative density of 90% of the theoretical density. In the final stage, the pores are pinch off and become isolated at the grain corners. In an idealized model, the pores are assumed to shrink continuously and may disappear altogether.

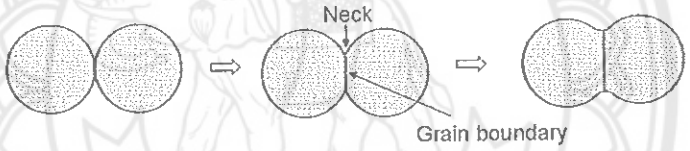

Figure 9 Schematic of two particles partly joined together on sintering process characterization techniques for ferroelectric ceramics [22]

Typical characterizations for ferroelectric ceramics

Thermal analysis (DSC and TGA)

The basis of Differential scanning calorimetry (DSC) is the measurement of heat flow which is plotted against the temperature of the furnace or the time to get a thermogram. The curve obtained in DSC is between dH/dt in $mJ \cdot s^{-1}$ or $mcal \cdot s^{-1}$ as a function of time or temperature. A typical DSC curve is shown in Figure 10. The deviation observed above the base (zero) line is called an exothermic transition and the deviation below is called endothermic transition. The area under the peak is directly proportional to the heat evolved or absorbed by the reaction, and the height of the curve is directly proportional to the rate of reaction

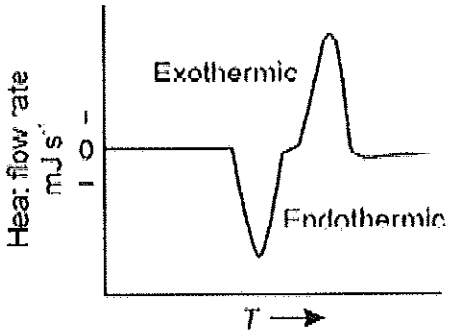

Figure 10 A typical DSC curve [24]

The block diagram of a DSC instrument as shown in Figure 11, essentially works on the temperature control of two similar specimen holder assemblies. The left half of the block diagram represents the circuit for differential temperature control while the right hand side represents average temperature control. In the average temperature control circuit, the temperature of the sample and reference are measured and averaged and the heat output of the average heater is automatically adjusted so that the average temperature of the sample and reference increases at a linear rate. The differential temperature control circuit monitors the difference in temperature between the sample and reference and automatically adjusts the power to either the reference or sample chambers to keep the temperatures equal. For getting a thermogram, the temperature of the sample is put on the *x*-axis and the difference in power supplied to the two differential heaters is displayed on the *y*-axis.

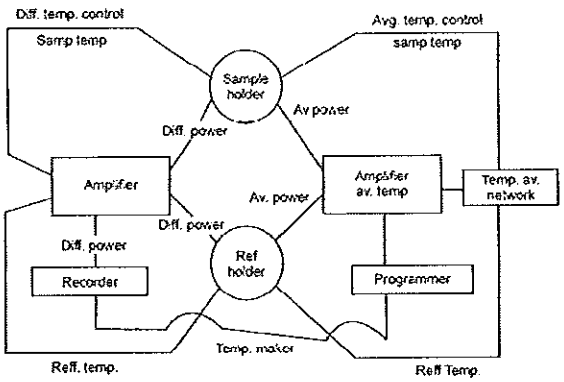

Figure 11 Block diagram of a DSC instrument [24]

Thermogravimetric analysis (TGA) is an analytical technique used to determine a material's thermal stability and its fraction of volatile components by monitoring the weight change that occurs as a specimen is heated. The measurement is normally carried out in air or in an inert atmosphere, such as Helium or Argon, and the weight is recorded as a function of increasing temperature. Sometimes, the measurement is performed in a lean oxygen atmosphere (1 to 5% O_2 in N_2 or He) to slow down oxidation. In addition to weight changes, some instruments also record the temperature difference between the specimen and one or more reference pans (differential thermal analysis, or DTA) or the heat flow into the specimen pan compared to that of the reference pan (differential scanning calorimetry, or DSC). The latter can be used to monitor the energy released or absorbed via chemical reactions during the heating process.

X-ray diffraction (XRD)

In X-ray diffraction, a collimated of mono-chromatic X rays between 0.5 – 2Å wavelength which strike a sample and are diffracted by the crystal planes present Bragg's law.

$$\lambda = 2d\sin\theta \qquad \text{[Eq.15]}$$

Bragg's law relates to the spacing between planes, d, to the diffraction angle, 2θ, which is scanned to pick up diffraction from the different crystal planes present. The azimuthal orientation of the diffraction beams also reveals the crystalline orientation. Distortions or broadening of the diffraction beams carry information on crystal strain and grain size. The schematic illustration of XRD analysis is illustrated in Figure 12.

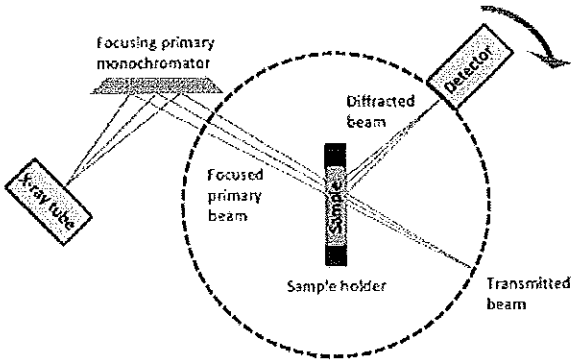

Figure 12 Schematic illustration of the diffractometer method of crystal analysis

Scanning electron microscope (SEM)

Scanning electron microscopy (SEM) is one of the most versatile and well known analytical techniques. Compared to a conventional optical microscope, an electron microscope offers advantages including high magnification, large depth of focus, great resolution and ease of sample preparation and observation. Electrons generated from an electron gun enter a surface of a sample and generate many low energy secondary electrons. The intensity of these secondary electrons is governed by the surface topography of the sample. An image of the sample surface is therefore constructed by measuring secondary electron intensity as a function of the position of the scanning primary electron beam. In addition to secondary electron imaging, backscattered electron imaging and Energy Dispersive X-ray (EDX) Analysis are also useful tools widely used for chemical analysis. The intensity of backscattered electrons generated by electron bombardment can be correlated to the atomic number of the element within the sampling volume. Hence, qualitative elemental information can be revealed. The characteristic X-rays emitted from the sample serve as fingerprints and give elemental information of the samples including semi-quantitative analysis, quantitative analysis, line profiling and spatial distribution of elements. A schematic diagram of the basic design of a SEM instrument is shown in Figure 13.

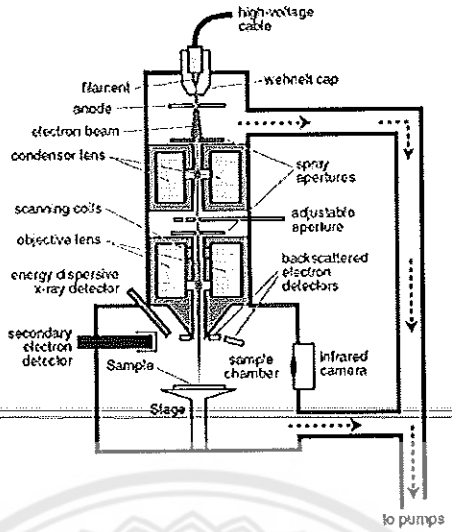

Figure 13 Schematic diagram of the basic design of a SEM [24]

Transmission electron microscope (TEM)

Figure 14 shows a schematic outline of a TEM. A TEM contains four parts: electron source, electromagnetic lens system, sample holder, and imaging system.

TEM works like a slide projector. A projector shines a beam of light which transmits through the slide. The patterns painted on the slide only allow certain parts of the light beam to pass through. Thus the transmitted beam replicates the patterns on the slide, forming an enlarged image of the slide when falling on the screen.

TEM works the same way except that they shine a beam of electrons (like the light in a slide projector) through the specimen (like a slide). However, in TEM, the transmission of the electron beam is highly dependent on the properties of the material being examined. Such properties include density, composition, etc. For example, porous material will allow more electrons to pass through while dense material will allow less. As a result, a specimen with a non-uniform density can be examined by this technique.

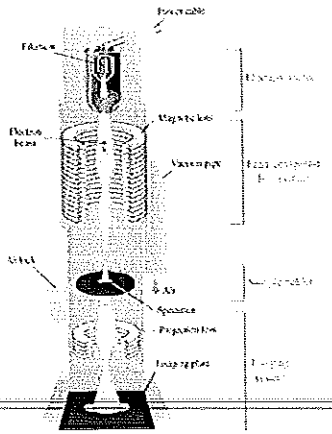

Figure 14 The schematic outline of a TEM [24]

Dielectric measurement

Parallel plate capacitor system uses a parallel plate capacitor as a sample holder, with the material under the test sandwiched between. This method requires an impedance analyzer or LCR meter. The measurements are at low frequencies, typically below 1 GHz. The material is stimulated by an AC source and the actual voltage across the material is monitored. The material test parameters are derived by knowing the dimensions of the material and by measuring its capacitance and dissipation factor. After putting a sample into a sample holder, a capacitor is formed. The parallel plate method involves sandwiching a thin sheet of material between two electrodes to form a capacitor. The measured capacitance is then used to calculate permittivity. The schematic diagram for this technique is shown in Figure 15.

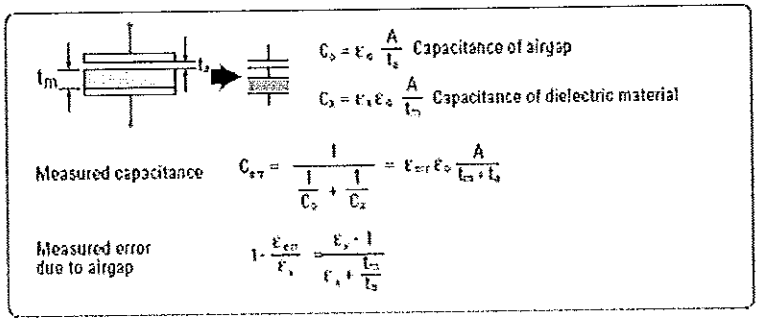

Figure 15 Diagram for dielectric measurement (parallel plate method) [24]

Ferroelectric measurement

A *P-E* loop for a device is a plot of the charge or polarization developed, against the electric field applied to that device (*E*) at a given frequency.

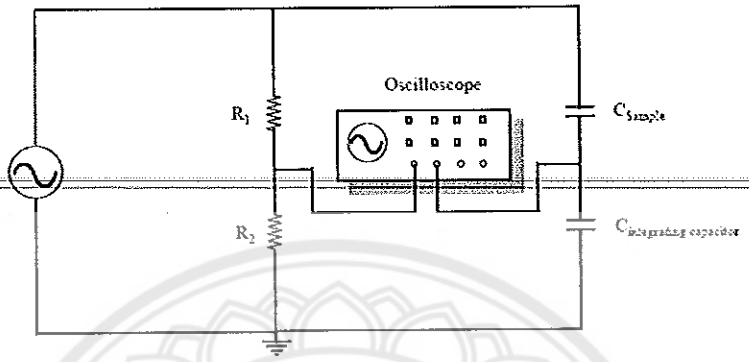

Figure 16 Schematic of a circuit for *P-E* measurement [24]

A schematic of the experimental setup is shown in Figure 16. Here the field applied across the sample is attenuated by a resistive divider, and the current is integrated into charge by virtue of a large capacitor in series with the sample. Both these voltages are then fed into the X and Y axes of an oscilloscope to generate the *P-E* loop. The applied voltage was usually a sinusoid at mains frequency as this was the simplest method to generate the required voltage and current.

CHARPTER III

LITERATURE REVIEWS

This chapter is composed of several reports whose topics relate to this work. The viewpoints of this section include: the effects of zirconium content on structure and typical properties of $Ba(Zr_xTi_{1-x})O_3$ system, various techniques for improving BNT-properties, and the application of the combustion technique for synthesizing ferroelectric ceramics.

Barium zirconium titanate

The substitution of Zr^{4+} to Ti^{4+} to form $Ba(Zr_xTi_{1-x})O_3$ or BZT became interesting for more fundamental studies and also for some novel applications due to its excellent dielectric, tunability and promising piezoelectric and relaxor properties. The ferroelectric properties of BZT are largely dependent on the amount of Zr^{4+} substitution. At room temperature, this ceramics show normal ferroelectric behavior for $0 < x < 0.20$ and relaxor behavior when $x > 0.25$ [25].

As mentioned, $BaTiO_3$ exhibits a cubic phase at high temperature. By decreasing the temperature, the crystal structure is slightly distorted. The first phase transition occurs at ~120 °C and is called Curie temperature (T_c), in which the structure changes from a cubic to a tetragonal structure [20]. The next phase transition point, defined as T_{o-t} (~ 0 °C), is the phase transition-temperature from a tetragonal to an orthorhombic structure [20]. At -90 °C, the crystal structure is transformed from orthorhombic to rhombohedral. This point is defined as T_{r-o} [20]. Substitution of Zr^{4+} to Ti^{4+} induces T_{r-o} and T_{o-t} to increase, whereas T_c decreases [8]. When the Zr content is ~15 at.%, all the above three phase transition temperatures T_{o-t}, T_{r-o} and T_c merge near room temperature as reported by Dixit et al. [25]. The schematic diagrams of phase transition temperatures shifted and pinch phase transition are shown in Figure 17(a) and (b), respectively.

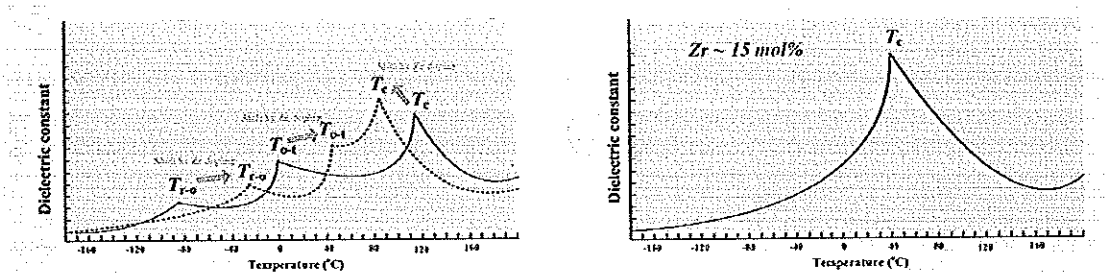

Figure 17 Schematic diagram of how the Zr doped affects the phase transition temperatures of barium titanate

Effects of zirconium content on structure and typical properties of BZT ceramics

1. **Crystal structure**

There are different reports about how the crystal structure of $BaTiO_3$ is changed due to Zr substitution [26, 27, 28, 29]. Some groups reported the crystal structure of $BaTiO_3$ shows a tetragonal phase and substitution of Zr caused the tetragonality to increase. Chen, et al. [27] studied the crystal structure of $Ba(Zr_xTi_{1-x})O_3$ with $0.05 \leq x \leq 0.20$. The result demonstrated that BZT exhibited a tetragonal structure in all compositions. By increasing zirconium substitution, the lattice parameter a was increased while the lattice parameter c decreased. For $Ba(Zr_xTi_{1-x})O_3$ with $x = 0.2$, a c/a ratio of around 1.01 was observed as shown in Figure 18. Huang *et al.* [30] investigated the structure of $Ba(Zr_xTi_{1-x})O_3$ with x lower than 15 mol% by using XRD patterns. The results suggested that by increasing the zirconium content, the lattice parameters a and c were increased and the tetragonality approached 1 at 15 mol% zirconium substitution. Neirman, et al. [31] has also pointed out that as zirconium increased, both lattice parameters c and a were increased because the larger Zr^{4+} ionic radius (0.087 nm) is larger than that of Ti^{4+} (0.068 nm). However, the ratio of c/a decreased and when the zirconium content was higher than 10 mol%, the lattice constant increased in direct proportion to the increasing zirconium content.

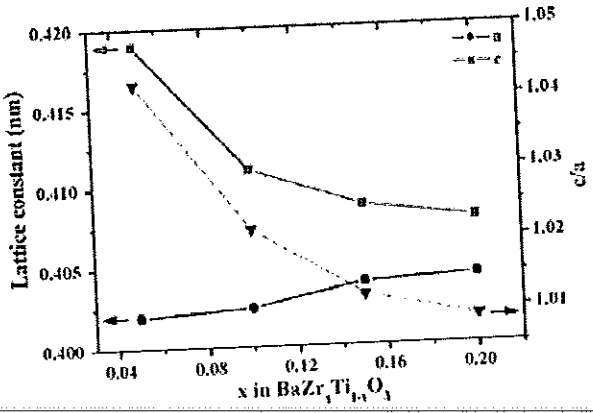

Figure 18 Dependences of the *a*- and *c*-axis lattice constants and *c/a* ratio (right hand side ordinate) on Zr/Ti ratio at room temperature [27]

Many researchers have reported the crystal structure of BZT from other viewpoints. Dixit, et al. [25] investigated the phase transition behavior of $Ba(Zr_xTi_{1-x})O_3$ with $0 \leq x \leq 0.4$. The report explained that the crystal structure of BZT depended upon the amount of Zr. BZT may have a tetragonal, orthorhombic, rhombohedral or cubic structure at room temperature. However, this report did not clearly explain the crystal structure of BZT for each composition. Kuang, et al. [29] studied the influence of Zr doped on properties of $Ba(Zr_xTi_{1-x})O_3$ with $0 \leq x \leq 0.12$. The report suggested that BZT exhibited a tetragonal phase at room temperature and that the crystal structure underwent a transformation from tetragonal to orthorhombic when zirconium content was increased. Binhayeeniyi, et al. [32] studied the crystal structure of $Ba(Zr_xTi_{1-x})O_3$ with $0 \leq x \leq 0.2$ using the Raman spectra and the XRD patterns. The report showed that is not possible to identify the crystalline phase of $Ba(Zr_xTi_{1-x})O_3$ with $0.00 \leq x \leq 0.02$ composition due to the close proximity of the diffraction angles. When the Zr content reached 10 mol%, the analysis results indicated that the crystal structure of BZT transformed from the orthorhombic to the rhombohedral phase and the structure was changed to a cubic phase when the zirconium content reached 20 mol%. The difference in the reports about the crystal structure of BZTx were summarized and are shown in Figure 19.

Report	x = 0-5	x = 5-10	x = 10-15	x = 15-20
[5], [6]	Tetragonal			
[8]	Orthorhombic	Tetragonal		
[9]	* Orthorhombic	Tetragonal		
[33]	Orthorhombic		Rhombohedral	

*Note: * = unidentified phase*

Figure 19 Phase identification of BZT ceramics with variation of mol% zirconium of x reported by several literatures

2. Dielectric constant

The substitution of Zr^{4+} to Ti^{4+} highly influenced the dielectric constant of $BaTiO_3$ [27, 29. However, the effects of zirconium content on the dielectric properties of BZT show different characteristics. Chen, et al. [27] investigated the temperature dependence of the dielectric permittivity of BZT ceramics with various stoichiometric percentages of zirconium from 5 to 20 mol% (Figure 20). The results demonstrated that the value of maximum permittivity decreased as the zirconium content increased. Meanwhile, the permittivity of BZT ceramics with a higher zirconium content exhibited broad peaks. The broadness indicated the diffuse phase transition from a ferroelectric to a paraelectric phase. Moreover, the diffuse transition behavior was enhanced with increasing zirconium content, indicating a composition induced diffuse transition. Yu, et al. [33] investigated the dielectric properties of $Ba(Zr_xTi_{1-x})O_3$ with $0 \leq x \leq 0.3$. The study showed permittivity displays an irregular change with variations of Zr concentration, and shows a maximum of 46,000 at a Zr concentration of $x = 0.08$ in region I (Figure 21). This might be partially related to its grain size variation, which depends on both the processing and Zr concentrations. The increase and decrease of the maximum dielectric constant due to an increase of the zirconium content as reported by other groups is exhibited and summarized in Figure 22.

Ferroelectric measurement

A *P-E* loop for a device is a plot of the charge or polarization developed, against the electric field applied to that device (*E*) at a given frequency.

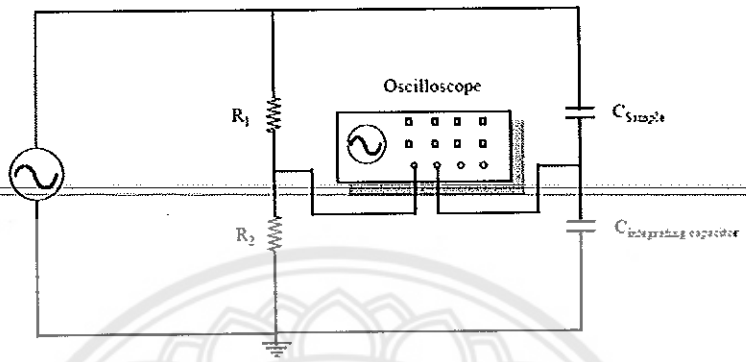

Figure 16 Schematic of a circuit for *P-E* measurement [24]

A schematic of the experimental setup is shown in Figure 16. Here the field applied across the sample is attenuated by a resistive divider, and the current is integrated into charge by virtue of a large capacitor in series with the sample. Both these voltages are then fed into the X and Y axes of an oscilloscope to generate the *P-E* loop. The applied voltage was usually a sinusoid at mains frequency as this was the simplest method to generate the required voltage and current.

CHARPTER III

LITERATURE REVIEWS

This chapter is composed of several reports whose topics relate to this work. The viewpoints of this section include: the effects of zirconium content on structure and typical properties of $Ba(Zr_xTi_{1-x})O_3$ system, various techniques for improving BNT-properties, and the application of the combustion technique for synthesizing ferroelectric ceramics.

Barium zirconium titanate

The substitution of Zr^{4+} to Ti^{4+} to form $Ba(Zr_xTi_{1-x})O_3$ or BZT became interesting for more fundamental studies and also for some novel applications due to its excellent dielectric, tunability and promising piezoelectric and relaxor properties. The ferroelectric properties of BZT are largely dependent on the amount of Zr^{4+} substitution. At room temperature, this ceramics show normal ferroelectric behavior for $0 < x < 0.20$ and relaxor behavior when $x > 0.25$ [25].

As mentioned, $BaTiO_3$ exhibits a cubic phase at high temperature. By decreasing the temperature, the crystal structure is slightly distorted. The first phase transition occurs at ~120 °C and is called Curie temperature (T_c), in which the structure changes from a cubic to a tetragonal structure [20]. The next phase transition point, defined as T_{o-t} (~ 0 °C), is the phase transition-temperature from a tetragonal to an orthorhombic structure [20]. At -90 °C, the crystal structure is transformed from orthorhombic to rhombohedral. This point is defined as T_{r-o} [20]. Substitution of Zr^{4+} to Ti^{4+} induces T_{r-o} and T_{o-t} to increase, whereas T_c decreases [8]. When the Zr content is ~15 at.%, all the above three phase transition temperatures T_{o-t}, T_{r-o} and T_c merge near room temperature as reported by Dixit et al. [25]. The schematic diagrams of phase transition temperatures shifted and pinch phase transition are shown in Figure 17(a) and (b), respectively.

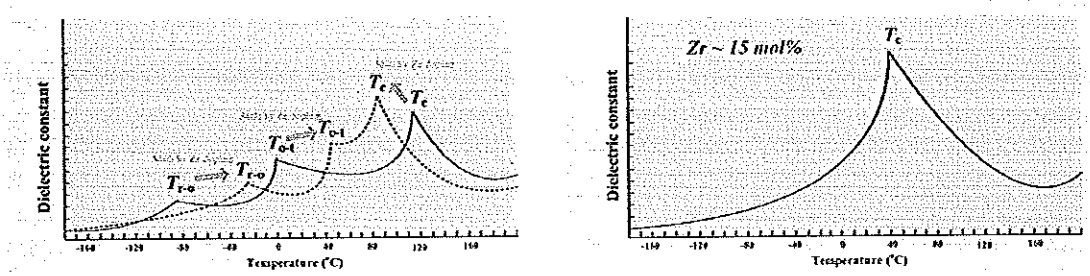

(a) (b)

Figure 17 Schematic diagram of how the Zr doped affects the phase transition temperatures of barium titanate

Effects of zirconium content on structure and typical properties of BZT ceramics

1. **Crystal structure**

There are different reports about how the crystal structure of $BaTiO_3$ is changed due to Zr substitution [26, 27, 28, 29]. Some groups reported the crystal structure of $BaTiO_3$ shows a tetragonal phase and substitution of Zr caused the tetragonality to increase. Chen, et al. [27] studied the crystal structure of $Ba(Zr_xTi_{1-x})O_3$ with $0.05 \leq x \leq 0.20$. The result demonstrated that BZT exhibited a tetragonal structure in all compositions. By increasing zirconium substitution, the lattice parameter a was increased while the lattice parameter c decreased. For $Ba(Zr_xTi_{1-x})O_3$ with $x = 0.2$, a c/a ratio of around 1.01 was observed as shown in Figure 18. Huang *et al.* [30] investigated the structure of $Ba(Zr_xTi_{1-x})O_3$ with x lower than 15 mol% by using XRD patterns. The results suggested that by increasing the zirconium content, the lattice parameters a and c were increased and the tetragonality approached 1 at 15 mol% zirconium substitution. Neirman, et al. [31] has also pointed out that as zirconium increased, both lattice parameters c and a were increased because the larger Zr^{4+} ionic radius (0.087 nm) is larger than that of Ti^{4+} (0.068 nm). However, the ratio of c/a decreased and when the zirconium content was higher than 10 mol%, the lattice constant increased in direct proportion to the increasing zirconium content.

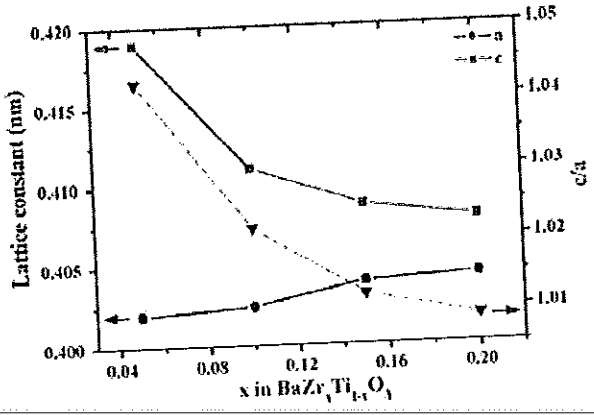

Figure 18 Dependences of the *a*- and *c*-axis lattice constants and *c/a* ratio (right hand side ordinate) on Zr/Ti ratio at room temperature [27]

Many researchers have reported the crystal structure of BZT from other viewpoints. Dixit, et al. [25] investigated the phase transition behavior of $Ba(Zr_xTi_{1-x})O_3$ with $0 \leq x \leq 0.4$. The report explained that the crystal structure of BZT depended upon the amount of Zr. BZT may have a tetragonal, orthorhombic, rhombohedral or cubic structure at room temperature. However, this report did not clearly explain the crystal structure of BZT for each composition. Kuang, et al. [29] studied the influence of Zr doped on properties of $Ba(Zr_xTi_{1-x})O_3$ with $0 \leq x \leq 0.12$. The report suggested that BZT exhibited a tetragonal phase at room temperature and that the crystal structure underwent a transformation from tetragonal to orthorhombic when zirconium content was increased. Binhayeeniyi, et al. [32] studied the crystal structure of $Ba(Zr_xTi_{1-x})O_3$ with $0 \leq x \leq 0.2$ using the Raman spectra and the XRD patterns. The report showed that is not possible to identify the crystalline phase of $Ba(Zr_xTi_{1-x})O_3$ with $0.00 \leq x \leq 0.02$ composition due to the close proximity of the diffraction angles. When the Zr content reached 10 mol%, the analysis results indicated that the crystal structure of BZT transformed from the orthorhombic to the rhombohedral phase and the structure was changed to a cubic phase when the zirconium content reached 20 mol%. The difference in the reports about the crystal structure of BZT*x* were summarized and are shown in Figure 19.

Report	x = 0-5	x = 5-10	x = 10-15	x = 15-20
[5], [6]	Tetragonal			
[8]	Orthorhombic	Tetragonal		
[9]	* Orthorhombic	Tetragonal		
[33]	Orthorhombic	Rhombohedral		

*Note: * = unidentified phase*

Figure 19 Phase identification of BZT ceramics with variation of mol% zirconium of x reported by several literatures

2. Dielectric constant

The substitution of Zr^{4+} to Ti^{4+} highly influenced the dielectric constant of $BaTiO_3$ [27, 29. However, the effects of zirconium content on the dielectric properties of BZT show different characteristics. Chen, et al. [27] investigated the temperature dependence of the dielectric permittivity of BZT ceramics with various stoichiometric percentages of zirconium from 5 to 20 mol% (Figure 20). The results demonstrated that the value of maximum permittivity decreased as the zirconium content increased. Meanwhile, the permittivity of BZT ceramics with a higher zirconium content exhibited broad peaks. The broadness indicated the diffuse phase transition from a ferroelectric to a paraelectric phase. Moreover, the diffuse transition behavior was enhanced with increasing zirconium content, indicating a composition induced diffuse transition. Yu, et al. [33] investigated the dielectric properties of $Ba(Zr_xTi_{1-x})O_3$ with $0 \leq x \leq 0.3$. The study showed permittivity displays an irregular change with variations of Zr concentration, and shows a maximum of 46,000 at a Zr concentration of $x = 0.08$ in region I (Figure 21). This might be partially related to its grain size variation, which depends on both the processing and Zr concentrations. The increase and decrease of the maximum dielectric constant due to an increase of the zirconium content as reported by other groups is exhibited and summarized in Figure 22.

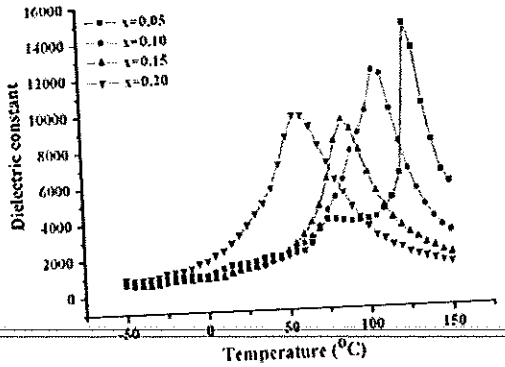

Figure 20 Temperature dependence of the relative permittivity of $Ba(Zr_xTi_{1-x})O_3$ ceramics at 1 kHz [27]

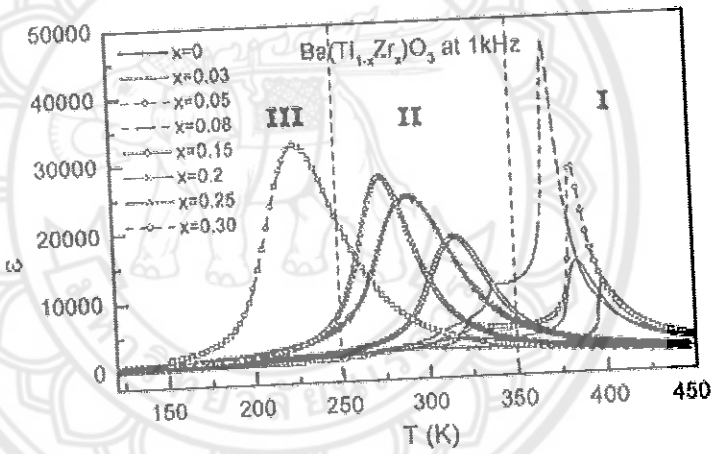

Figure 21 Temperature dependence of dielectric constant ε at 1 kHz for the $Ba(Zr_xTi_{1-x})O_3$ ceramics with x = 0, 0.03, 0.05, 0.08, 0.15, 0.2, 0.25 and 0.3 [33]

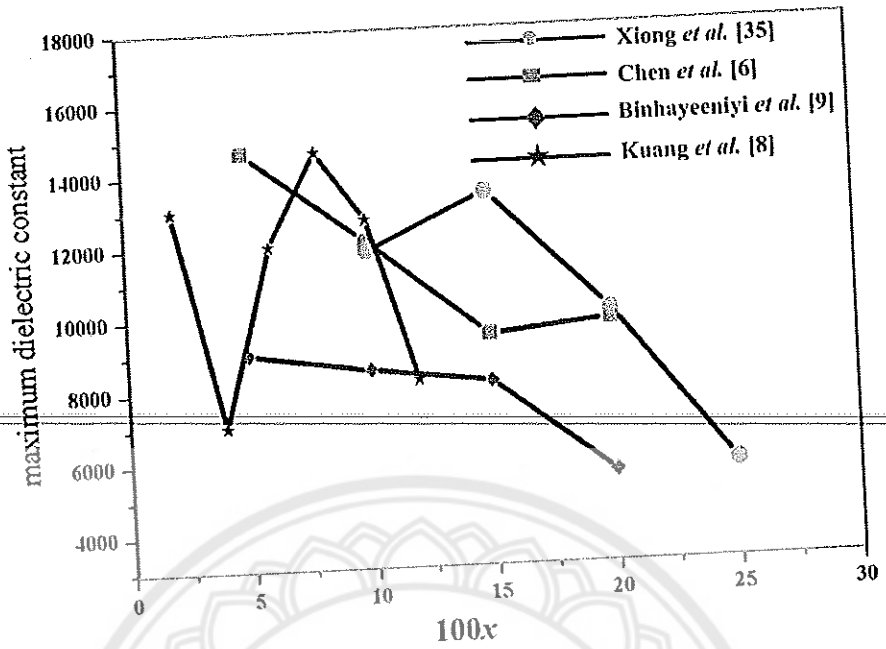

Figure 22 Variation of maximum dielectric constant of $Ba(Zr_xTi_{1-x})O_3$ from the literatures

3. Phase transition temperatures

The transition temperature of $BaTiO_3$ can be shifted when doped with isovalent ions substitution. Ba^{2+} can be replaced by isovalent ions with r_{12} radii between 130 and 160 pm (such as Pb^{2+}, Sr^{2+} and Ca^{2+}). Ti^{4+} can be replaced by isovalent ions with r_6 radii between 60 and 75 pm (such as Zr^{4+} and Sn^{4+}). For Ti^{4+} replaced by Zr^{4+}, they reduce T_c but raise the temperature of the other two transitions [32].

Nanakorn, et al. [33] studied the phase transition temperature of $Ba(Zr_xTi_{1-x})O_3$ ceramics with $0.00 \leq x \leq 0.08$ from the temperature dependence of the dielectric curve as shown in Figure 23. They found that with increasing Zr content (0–5 mol %), the transition temperatures from tetragonal to orthorhombic structure (T_1) shifts toward higher temperatures. Transition temperatures from orthorhombic to rhombohedral (T_2) are clearly shown only at $x = 0.05$. At $x = 0.08$, the diffuse phase transition occurs resulting in an unclear phase transition temperature (T_1 and T_2). The transition temperatures and Curie temperatures of the BZT based compositions were recorded and are summarized in Table 1.

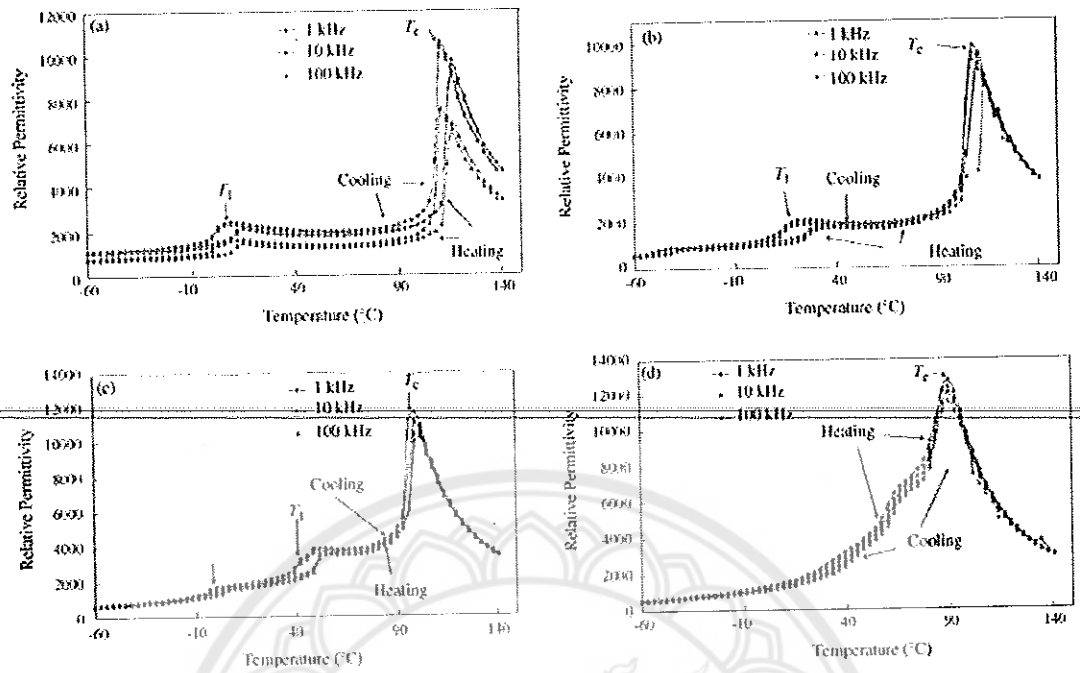

Figure 23 Temperature dependence of the relative permittivity for $Ba(Zr_xTi_{1-x})O_3$ ceramics with (a) $x = 0$ sintered at 1300 °C, (b) $x = 0.02$ sintered at 1350 °C, (c) $x = 0.05$ sintered at 1450 °C and (d) $x = 0.08$ sintered at 1400 °C at 1 kHz, 10 kHz and 100 kHz [32]

Table 1 The phase transition temperature (T_1, T_2 and T_c) of BZT ceramics [10]

$Ba(Zr_xTi_{1-x})O_3$	T_1 (°C)	T_2 (°C)	T_c (°C)
$x = 0.00$	6	-	117
$x = 0.02$	18	-	111
$x = 0.05$	42	0	102
$x = 0.08$	-	-	90

Kuang, et al. [29] plotted T_c (phase transition temperature from tetragonal to cubic structure), T_{o-t} (phase transition temperature from orthorhombic to tetragonal structure) and ε_m (maximum dielectric permittivity) as a function of zirconium content at 10 kHz for $Ba(Zr_xTi_{1-x})O_3$ ceramics with $0 < x < 0.12$ (Figure 24). The T_{o-t}

increased nonlinearly from 33 to 80 °C with increasing x from 0.02 to 0.10, respectively. Furthermore, the T_{o-t} peak decreased with increasing x. The phenomenon of decreasing T_c with increasing x can be explained in two ways. The first is because the radius of the Zr^{4+} is larger than that of the Ti^{4+} ion. The substitution of Zr^{4+} for Ti^{4+} will weaken the bonding force between the B-site ion and the oxygen ion of the ABO_3 perovskite structure. As the B–O bonds are weakened, the B-site ion can resume its position only when the tetragonal ferroelectric is at lower temperature, so the phase transition temperature is reduced. The second reason is because the weakening of the B–O bonds leads to a weaker distortion of the octahedron and the replacement also might induce a break of the cooperative vibration of the B–O chains. When this happens the c/a ratio is decreased. This break is responsible for the T_c of the BZT system, and thus a drop in Curie temperature was observed [8]. The values of T_c and T_{o-t} approached the same value when x is raised to ~0.12. The phase transition temperature from rhombehedral to orthorhombic (T_{r-o}), phase transition temperature from orthorhombic to tetragonal (T_{o-t}) and Curie temperature (T_c) dependence with zirconium content observed from literatures are listed in Table 2.

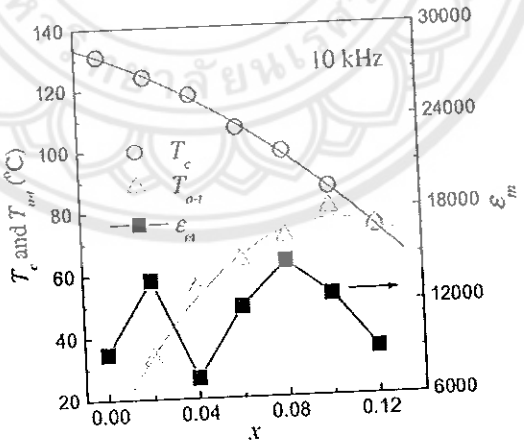

Figure 24 Phase transition temperature T_c, T_{o-t} and maximum dielectric permittivity ε_m as functions of zirconium content x at 10 kHz for $Ba(Zr_xTi_{1-x})O_3$ ceramics [29]

Table 2 $T_{r\text{-}o}$, $T_{o\text{-}t}$ and T_c as a function of zirconium content reported by literatures

Report	Composition of 100x of $Ba(Zr_xTi_{1-x})O_3$	$T_{r\text{-}o}$ (°C)	$T_{o\text{-}t}$ (°C)	T_c (°C)
Chen, et al.[6]	5			102
	10			89
	15			74
	20			55
Xiong, et al.[35]	10			90
	15			70
	20			40
	25			0
Kuang, et al.[8]	2		30	125
	4		55	118
	6		65	109
	8		70	100
	10		81	901
	12		75	75
Yu, et al.[34]	3	-33	27	107
	5	-13	47	102
	8	37	57	92
	15	-	-	37
	20	-	-	17
	25	-	-	-3
	30	-	-	-53

4. Ferroelectric polarization

The effects of zirconium content on the ferroelectric properties of BZT were investigated by Chen, et al. [6]. The results of well-behaved hysteresis loops of $Ba(Zr_xTi_{1-x})O_3$ with x = 0.05, 0.10, 0.15 and 0.20 are shown in Figure 25. It was found that the *P-E* hysteresis loop showed slimmer characteristics when the zirconium content increased.

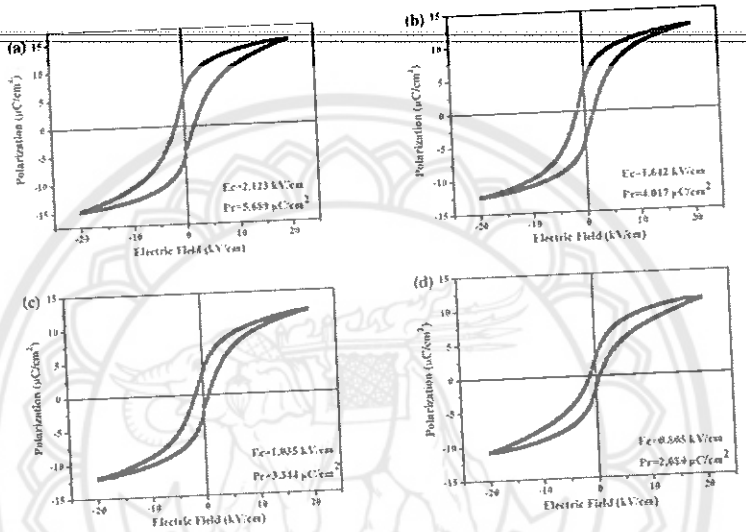

Figure 25 ***P-E*** **Hysteresis loops of $Ba(Zr_xTi_{1-x})O_3$ ceramics at room temperature and 1 kHz with (a) x = 0.05, (b) x = 0.10, (c) x = 0.15, and (d) x = 0.20** [27]

Figure 26 shows the plot of the coercive electric field (E_c) and the remanent polarization (P_r) versus the stoichiometric percentage of zirconium. Both E_c and P_r decreased as zirconium content increased. Variation in remanent polarization in BZT ceramics can be explaine by the difference of radius in Zr^{4+} and Ti^{4+}. The decrease in E_c values with increasing zirconium content could be attributed to the increase in grain size as a result of the same sintering temperature. It is well known that a reversal polarization process in the ferroelectric domain is much easier inside a large grain than in a small grain.

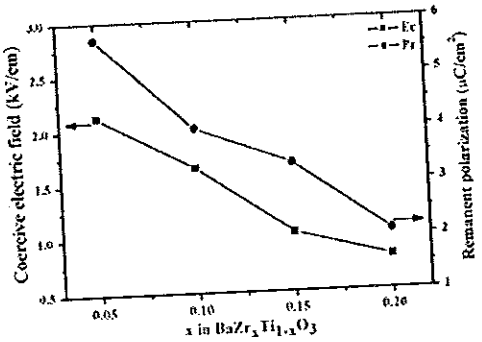

Figure 26 The E_c and P_r dependences of Zr/Ti ratio in $Ba(Zr_xTi_{1-x})O_3$ ceramics [6]

Nanakorn, et al. [10] investigated the effect of zirconium content and temperature on the *P-E* hysteresis loop of $Ba(Zr_xTi_{1-x})O_3$ ceramics with $0.00 \leq x \leq 0.08$. The report demonstrated that the loop altitude of the *P–E* hysteresis loops decreased with an increase in temperature when the temperature was raised and approached the Curie point (Figure 27). The variable of saturated polarization, remanent polarization and coercive field due to changing in zirconium content were listed in Table 3.

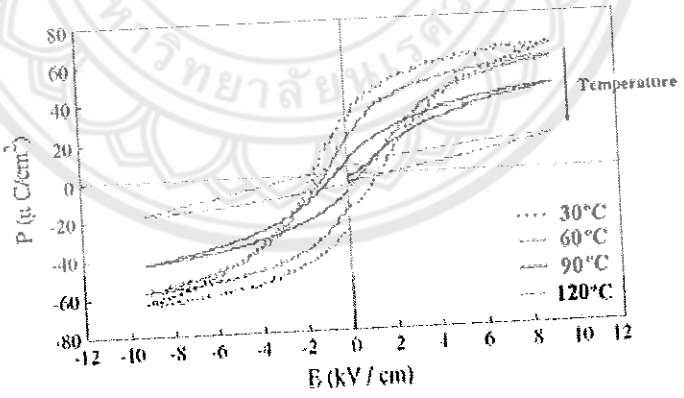

Figure 27 *P-E* hysteresis loop at the temperatures ranging from 30 °C to 120 °C of $BaZr_xTi_{1-x}O_3$ with $x = 0.08$ sintered at 1400 °C [33]

Table 3 The saturated polarization (P_s), remanent polarization (P_r), and coercive field (E_c) of BZT ceramics at 30 °C[33]

$Ba(Zr_xTi_{1-x})O_3$	P_s (μC/cm^2)	P_r (μC/cm^2)	E_c (kV/cm)
$x = 0.00$	35.862	4.424	0.696
$x = 0.02$	12.324	2.143	0.912
$x = 0.05$	57.920	25.033	1.048
$x = 0.08$	63.320	29.451	1.344

Bismuth sodium titanate ($Bi_{0.5}Na_{0.5}TiO_3$, BNT)

Bismuth sodium titanate ($Bi_{0.5}Na_{0.5}TiO_3$, BNT) was discovered by Smolensky, et al. in 1960 [36]. In pure BNT, half of all A-site positions are placed by bismuth (3^+) ions and the other half with sodium (1^+) ions. The B-site positions are placed by titanium (4^+) ions. Even though bismuth and sodium have very different charges, there is only a short range ordering of the A-site ions [34-36].

Pure BNT is a rhombohedral ferroelectric at room temperature. The rhombohedral-tetragonal phase transition temperature and Curie temperature are 300 and 540 °C, respectively [37]. The curves of permittivity versus temperature of BNT display a very interesting hump anomaly around 185 °C. This temperature is called the depolarization temperature (T_d), which corresponds to the transition from a ferroelectric to an anti-ferroelectric state. The maximum permittivity occurs around 340 °C, which is defined as T_m [35]. However, the phase transition behaviors at T_d and T_m are complicated and are not yet fully understood [35, 37].

BNT is one of the most important lead-free piezoelectric materials with a perovskite structure because of its high ferroelectricity ($P_r = 38\ \mu C/cm^2$) [36]. However, pure BNT piezoelectric ceramics are difficult to pole because of their relatively large coercive field (E_c = 73 kV/cm) and high electrical conductivity. It for this reason that ways to improve the production of pure BNT have been extensively studied.

Several techniques for improvement of BNT properties

1. Cation substituted BNT perovskite lattices

Yang, et al. [42] mentioned BKT doped to BNT for 16-20 mol% induce the morphotopic phase boundary (MPB) between rhombohedral–tetragonal, which enhanced the electrical properties of BNT. Thus, this group was investigated to discover the effects of $Bi_{0.5}K_{0.5}TiO_3$ (BKT) content on the phase structure, microstructure, dielectric and piezoelectric properties of BNT-xBKT ceramics with 0.1 $\leq x \leq 0.2$. The samples were prepared via the solid-state reaction method, which were calcined and sintered at 850 °C and 1150-1200 °C, respectively. The crystal structure was studied using XRD pattern as shown in Figure 28.

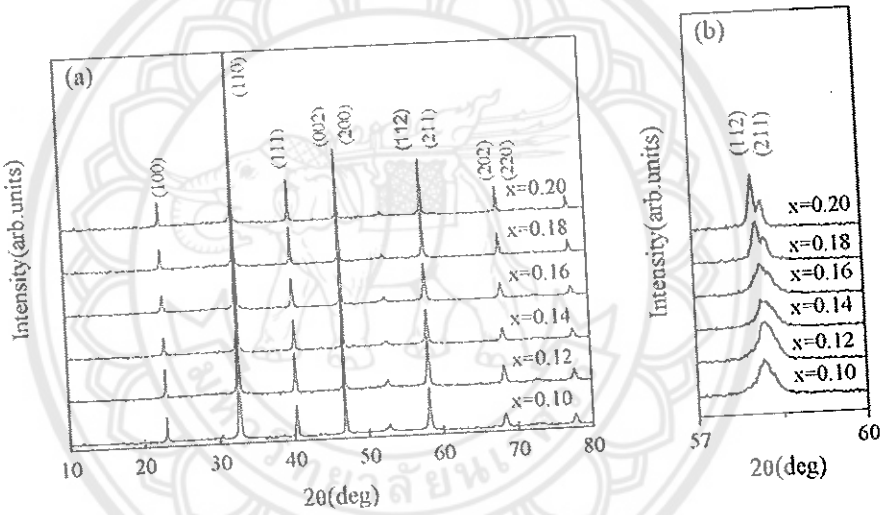

Figure 28 XRD patterns of BNT-xBKT powders [42]

From the XRD results, it can be clearly seen that the single peak of (211) at 2θ of 57° - 60° can be detected when $x < 0.16$. This suggests that the samples exhibit a rhombohedral structure. When $x = 0.16$, the diffraction peak begins to split. The (211) peak splits out to (211), (112), which indicates that the crystal was transformed to a tetragonal phase when $x = 0.18$ and 0.20. It can be concluded that the MPB is located at $0.16 \leq x \leq 0.20$. The results of the piezoelectric constant (d_{33}), electromechanical coupling factor (K_p), dielectric constant at room temperature (ε_r) and tanδ as a function of BKT content are shown in Figure 29. The results suggest that the electrical properties of BNT-xBKT ceramics tended to enhance by the increasing of x. The

maximums of d_{33} and K_p were obtained at $x = 0.18$ with the values of 144 pC/N and 0.29, respectively. This is because this composition is located near the MPB region.

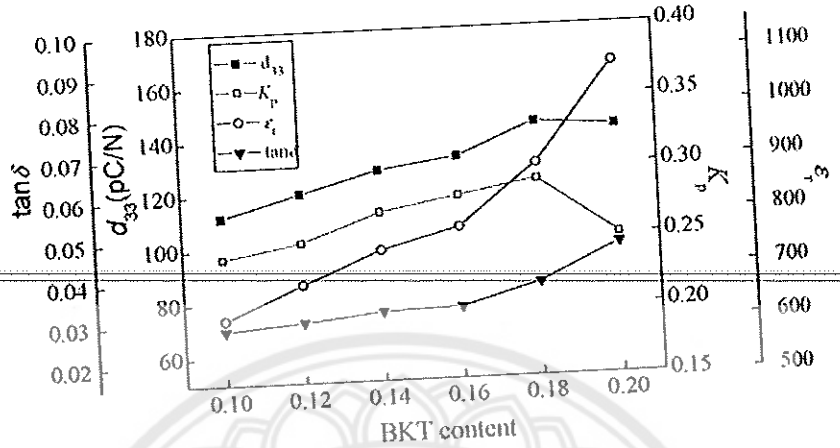

Figure 29 The piezoelectric constant d_{33}, electromechanical coupling factor K_p, dielectric constant at room temperature ε_r and tanδ as a function of BKT content [42]

Figure 30 shows the temperature dependence of ε_r and tanδ of BNT-xBKT ceramics measured at 1 kHz. There are two abnormal dielectric peaks in all samples with different compositions. The appearance of the first peak at T_t is caused when the phase is transformed from rhombohedral ferroelectric to tetragonal anti-ferroelectric. The appearance of the second peak at T_c can be explained by the transition from a tetragonal anti-ferroelectric to cubic paraelectric phase. It can be observed that the T_t shifts to lower temperature regions and the T_c shifts to higher temperature regions with increasing BKT content.

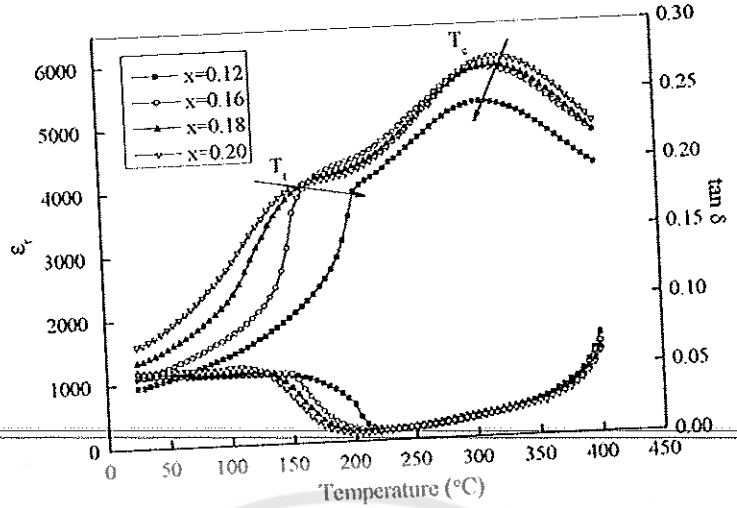

Figure 30 The temperature dependence of ε_r and tanδ of BNT-xBKT ceramics with different compositions [42]

The other some cation substituted to the A-site of BNT ceramics to improve BNT properties was the Li^{1+} ion. Lu, et al. [12] investigated the effects of Li and K being substituted in a BNT solid solution and recorded the effects on the crystal structure, dielectric properties and piezoelectric properties. The XRD patterns of the Li and K substituted BNT samples in the 2θ range of 20–70° and 38–50° are shown in Figure 31.

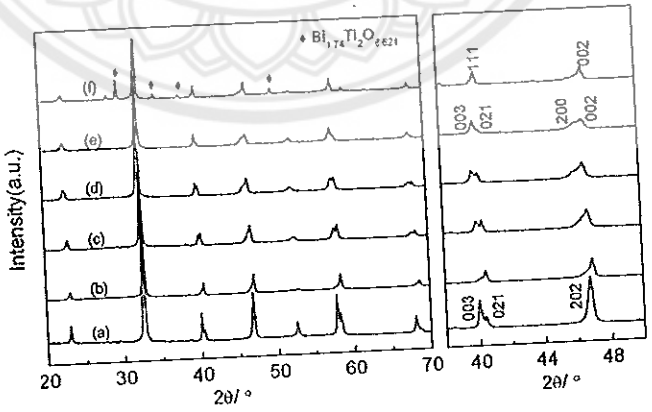

Figure 31 XRD patterns of Li and K substituted BNT ceramics; (a) BNT, (b) BNLT10, (c) BNKT10, (d) BNKT16, (e) BNKLT16-10 and (f) BNKLT16-35, in the 2θ range of 20–70° and 38–50°[12]

Generally, the symmetry of BNT at room temperature is a rhombohedral structure. This can be characterized by the splitting of (003)/(021) peaks at around 2θ of 40° and a single peak of (202) at around 2θ of 46.5°. $Bi_{0.5}K_{0.5}TiO_3$ is a perovskite type structure with tetragonal symmetry at room temperature which is characterized by the splitting of the (002)/(200) diffraction peaks at 2θ of 46.5°. The study results indicated that BNT, BNLT10 and BNKT10 have the same structure with a rhombohedral symmetry. The BNKT16 and BNKLT16-10 show the coexistence phases of a rhombohedral-tetragonal structure. With a further increase of Li content, the BNKLT16-35 shows a cubic structure and is accompanied with a secondary phase of $Bi_{1.74}Ti_2O_{6.624}$.

Figure 32 shows the temperature dependences of permittivity for Li and/or K substituted BNT ceramics at a frequency of 10 kHz. The permittivity of K doped BNT (BNKT16) ceramics is larger than that of BNT in the range of measurement temperature, especially the maximum permittivity. For Li doped BNT (BNLT10) ceramics, the permittivity is similar to pure BNT but is less than that of BNT when the temperature is higher than 200 °C. Moreover, the permittivity of K and Li doped BNT (BNKLT16-10) ceramics shows the mixing characteristics of K and Li doped BNT.

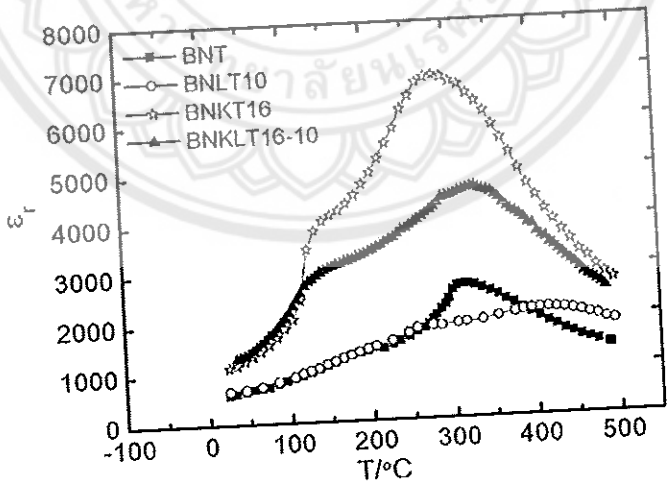

Figure 32 Temperature dependences of permittivity for Li and K substituted BNT ceramics at a frequency of 10 kHz [12]

The dielectric and piezoelectric properties of typical compositions of Li and K substituted BNT ceramics at room temperature are shown in Table 4. Li and/or K replacement for Na in BNT are improve the dielectric and piezoelectric properties, especially for the BNKLT1610 (near MPB) composition.

Table 4 Room-temperature dielectric and piezoelectric properties of BNT-based ceramics [12]

Compositions	BNT	BNLT10	BNKT10	BNKT16	BNKLT16-10
Piezoelectric constant d_{33} (pC/N)	78	95	105	138	160
Electromechanical coupling coefficient (k_p)	0.16	0.18	0.25	0.30	0.35
Dielectric permittivity ε_r at 25°C, 1 kHz	420	480	521	1020	1080
Dielectric loss $\tan\delta$ at 25°C, 1 kHz	0.03	0.036	0.023	0.029	0.038
Depolarization temperature, T_d (°C)	205	245	175	135	125
Curie temperature, T_C (°C)	315	365	285	295	335

2. Binary system of BNT-based

Chu, et al. [43] attempted to improve the electrical properties of BNT by investigating the MPB composition of the BNT-BT binary system. (1-x)$Na_{0.5}Bi_{0.5}TiO_3$–$xBaTiO_3$ with x = 0.02, 0.04, 0.06, 0.08 and 0.10 (abbreviated as NBBTx, x = 2, 4, 6, 8 and 10) were prepared via the conventional method. The X-ray diffraction patterns of the prepared samples are shown in Figure 33.

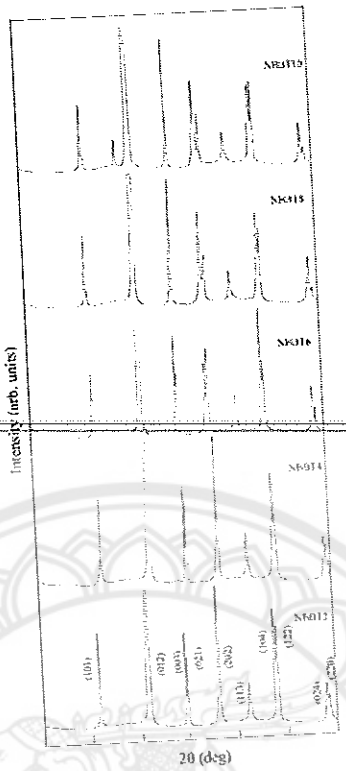

Figure 33 X-ray diffraction patterns of (1-x)$Na_{0.5}Bi_{0.5}TiO_3$–$xBaTiO_3$ ceramics[43]

At room temperature, the crystal structure of BNT is rhombohedral and that of BT is tetragonal. The X-ray diffraction revealed that NBBT2 and NBBT4 ceramics were in a rhombohedral phase. With increasing amount of $BaTiO_3$, the structures of NBBT8 and NBBT10 ceramics turned into a tetragonal symmetry characterized by (003) and (021) peaks combining into one peak and (202) peak splitting. The NBBT6 ceramics feature both rhombohedral and tetragonal symmetry. Therefore the MPB of (1-x)$Na_{0.5}Bi_{0.5}TiO_3$–$xBaTiO_3$ system is near $x = 0.06$.

The detailed electrical properties of NBBTx ceramics are shown in Table 5. The electrical properties of the (1-x)$Na_{0.5}Bi_{0.5}TiO_3$–$xBaTiO_3$ system, such as electromechanical coupling coefficient, piezoelectric constant and dielectric constant vary with the amount of $BaTiO_3$ and suggests that NBBT6 is the MPB composition.

Table 5 Electrical properties of (1-x)$Na_{0.5}Bi_{0.5}TiO_3$–$xBaTiO_3$ or NBBTx ceramics [43]

Property		Materials				
		NBBT2	NBBT4	NBBT6	NBBT8	NBBT10
Coupling factor	k_t	0.46	0.45	0.40	0.42	0.41
	k_p	0.20	0.21	0.29	0.13	0.14
Piezoelectric constant	d_{33}	78	87	122	112	94
Dielectric constant	ε^T_{33}	402	445	601	841	764
Frequency constant (Hz.m)	N_p	3190	3000	3000	2950	2980
	N_t	2680	2570	2522	2375	2418
Poisson ratio	σ	0.26	0.25	0.25	0.25	0.24
Dielectric loss	tgδ	0.0173	0.0207	0.0179	0.0204	0.0239
Maximum temperature of ε (°C)	T_m	265	230	225	250	180
Depolarization temperature (°C)	T_d	180	165	100	140	170
Remnant polarization(μC/cm²)	P_r	37	-	40	36	22.5
Corecive field (V/mm)	E_c	4700	-	2880	3200	2880

Peng, et al. [44] studied the $(Bi_{0.5}Na_{0.5})TiO_3$ (BNT)-$Ba(Zr_{0.05}Ti_{0.95})O_3$ (BZT) binary system for (1-x)BNT–BZT100x with $x \leq 0.12$. The investigation focused on searching for MPB composition between BNT (rhombohedral) and BZT (tetragonal).

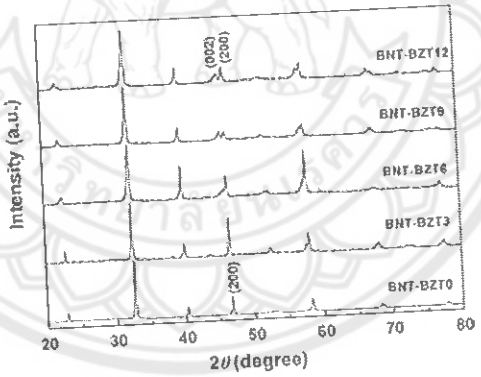

Figure 34 XRD patterns of BNT-BZT100x ceramics [44]

The X-ray diffraction patterns of BNT-BZT100x are shown in Figure 34. The splitting of (002)/(200) peaks from the single (200) peak showed that the crystal structure is transformed from rhombohedral to tetragonal due to an increase of BZT content. Moreover, the diffraction pattern of BNT-BZT9 suggested this has a MPB composition.

The $P-E$ hysteresis loops of the BNT-BZT ceramics a room temperature are shown in Figure 35. The results indicated that the BZT content highly influences the

ferroelectric properties of the system. The highest remanent polarization was exhibited in the BNT-BZT9 composition and it was near the MPB region

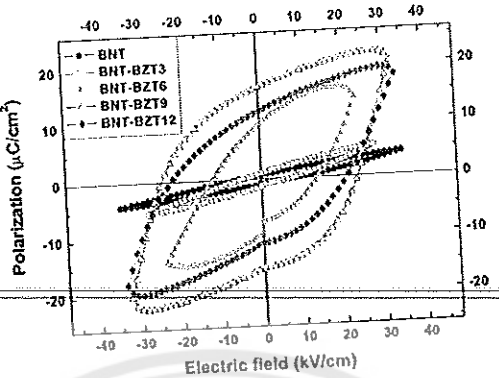

Figure 35 *P-E* **loops of BNT–BZT100*x* ceramics with a maximum field of 40 kV/cm at room temperature [44]**

The piezoelectric constant (d_{33}) and dielectric constant ($\varepsilon_{33}^{T}/\varepsilon_0$) of BNT–BZT ceramics altered with BZT fraction are listed in Table 6. The piezoelectric constant (d_{33}) increases with an increased BZT fraction up to 9 mol% and then decreases. The dielectric constant changes as a function of composition similarly to the piezoelectric constant, with a maximum value of 881.4 at 9 mol% BZT. The XRD pattern, piezoelectric and dielectric properties results support that BNT-BZT9 has a rhombohedral-tetragonal phase near the morphotropic phase boundary MPB.

Table 6 Piezoelectric, dielectric properties and density of BNT–BZT100*x* ceramics [44]

	d_{33} (pC/N)	T_c (°C)	ρ (g/cm³)	$\varepsilon_{33}^{T}/\varepsilon_0$	tan δ (%)
BNT	64	310	5.32	302.6	1.752
BNT-BZT3	79	236	5.76	345.6	1.765
BNT-BZT6	107	236	5.72	844.6	2.185
BNT-BZT9	147	244	5.82	881.4	2.636
BNT-BZT12	112	259	5.69	788.7	2.980

Investigation of the combustion technique for synthesizing ferroelectric materials

1. Typical organic compound selection as fuel

Hwang, et al. [20] investigated preparation of electronic ceramic oxide powders through the combustion technique. The organic compounds (e.g., glycine, urea, citric acid, alanine, or carbohydrazide) were mixed directly with the raw materials to synthesize $Ni_{0.5}Zn_{0.5}Fe_2O_4$ powders. Some of the properties of the five selected fuel types (alanine, glycine, carbohydrazine, urea, and citric acid) are listed in the Table 7.

Table 7 Some properties of organic compounds [20]

Properties	Organic component				
	Alanine	Glycine	Carbohydrazide	Urea	Citric acid
Structural formula		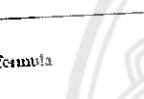		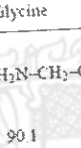	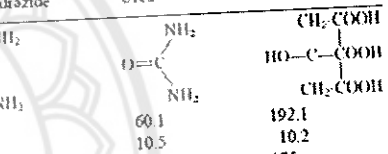
Molecular weight (g/mol)	80.1	90.1	75.1	60.1	192.1
Heat of combustion (kJ/g)	18.2	13.0	12.6	10.5	10.2
Decomposition temperature (°C)	314	262	153	135	175

The raw materials and organic fuel were mixed together in an equivalent stoichiometric ratio. The thermogravimetric analysis (TGA) of the precursor was investigated and is illustrated in Figure 36. Some organic fuels such as chabohydrazide and glycine showed that the slope of the weight loss–temperature curve was very steep. This indicated that the decomposition reaction of the fuel took place very rapidly. In case of citric acid, a distinct of three-stage weight loss was observed. When compared with other organic fuels, the slope of this curve is relatively flat which indicated that the reaction is more moderate. The analytical results obtained from synthesizing Ni–Zn ferrite products using various organic fuels is listed in Table 8. The results demonstrated that the combustion technique produces nanocrystalline and good chemically homogeneitic powders.

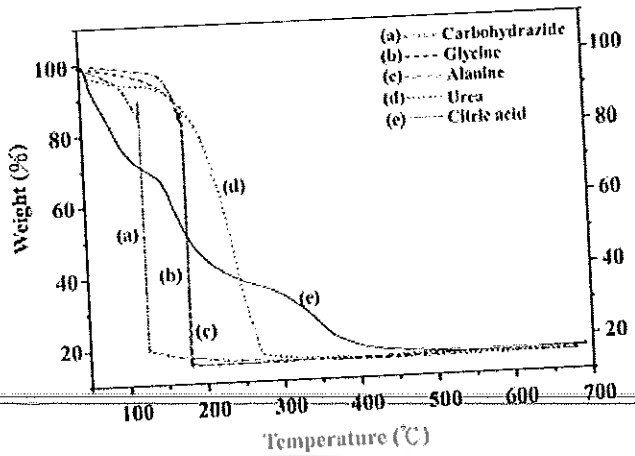

Figure 36 Typical TGA plots of the precursors prepared by using various fuels [20]

Table 8 Effects of various organic compounds and particular properties of Ni–Zn ferrite synthesized by the proposed combustion synthesis method [20]

Fuel	T_m[a] (°C)	Amount of gas produced (mole)	Crystallite size[b] (nm)	Surface area (m^2/g)	Carbon content (wt.%)	$Ni^{2+}:Zn^{2+}:Fe^{3+}$ (molar ratio)	M_s[c] (Am^2/kg)
Alanine	1245	20.7	38.6	24.7	1.64	0.500:0.467:1.920	60.8
Glycine	1150	26.2	32.7	31.2	1.53	0.500:0.471:1.922	62.4
Carbohydrazide	1380	24.0	43.7	20.6	1.87	0.500:0.462:1.917	58.5
Urea	785	30.7	20.2	48.5	3.82	0.500:0.483:1.936	57.2
Citric acid	725	26.2	22.7	44.1	5.75	0.500:0.490:1.947	55.8

2. Decomposition reaction of the typical fuel (urea)

Eichelbaum, et al. [45] studied the decomposition reaction of urea using simultaneous thermogravimetric (TG), differential thermal analysis (DTA) and measured the gasses produce. The results are shown in Figure 37.

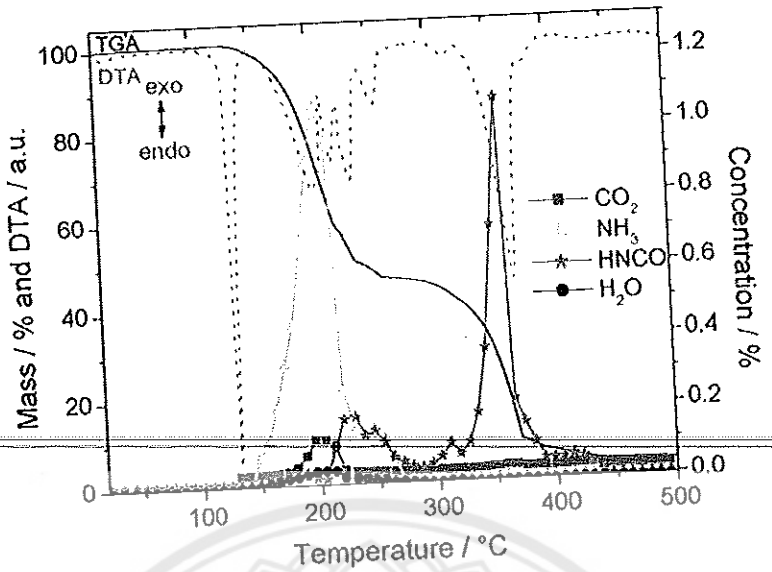

Figure 37 TGA, DTA graphs and quantitative results of the GC/MS evolved gas analysis [45]

The results revealed that the decomposition reactions of urea show multi-stages. Urea initially melted at 133 °C and then several decomposition reactions occurred between 150-250 °C. The main reaction consisted of the thermolysis of urea to ammonia (NH_3) and isocyanic acid (HNCO). However, only a minor amount of HNCO was detected between 210 and 270 °C. The weak production of CO_2 at 200 °C can be explained by the hydrolysis of HNCO with trace water in the original sample to NH_3 as shown in Figure 38(a). The other main reactions in this temperature range were the formation of ammelide. This started with the reaction between HNCO and urea to form biuret at a temperature higher than 150 °C and then the biuret reacted with HNCO to form ammelide as shown in Figure 38(b). Above 270 °C, cyanuric acid was formed from HNCO (Figure 38(c)). A large mass loss can be observed in the TGA spectrum (Figure 37) accompanied with a sharp endothermic peak at 370 °C and the production of large amounts of HNCO. This can be explained by the thermolysis of cyanuric acid, which decomposes above 300 °C (Figure 38(c)). At the same time, ammelide reacted with NH_3 and ammeline was formed at temperature higher than 270 °C (Figure 38(d)). Thereafter, the ammeline continuously decomposed to HNCO and cyanogens (CN_2) at high temperature as shown in Figure 38(e).

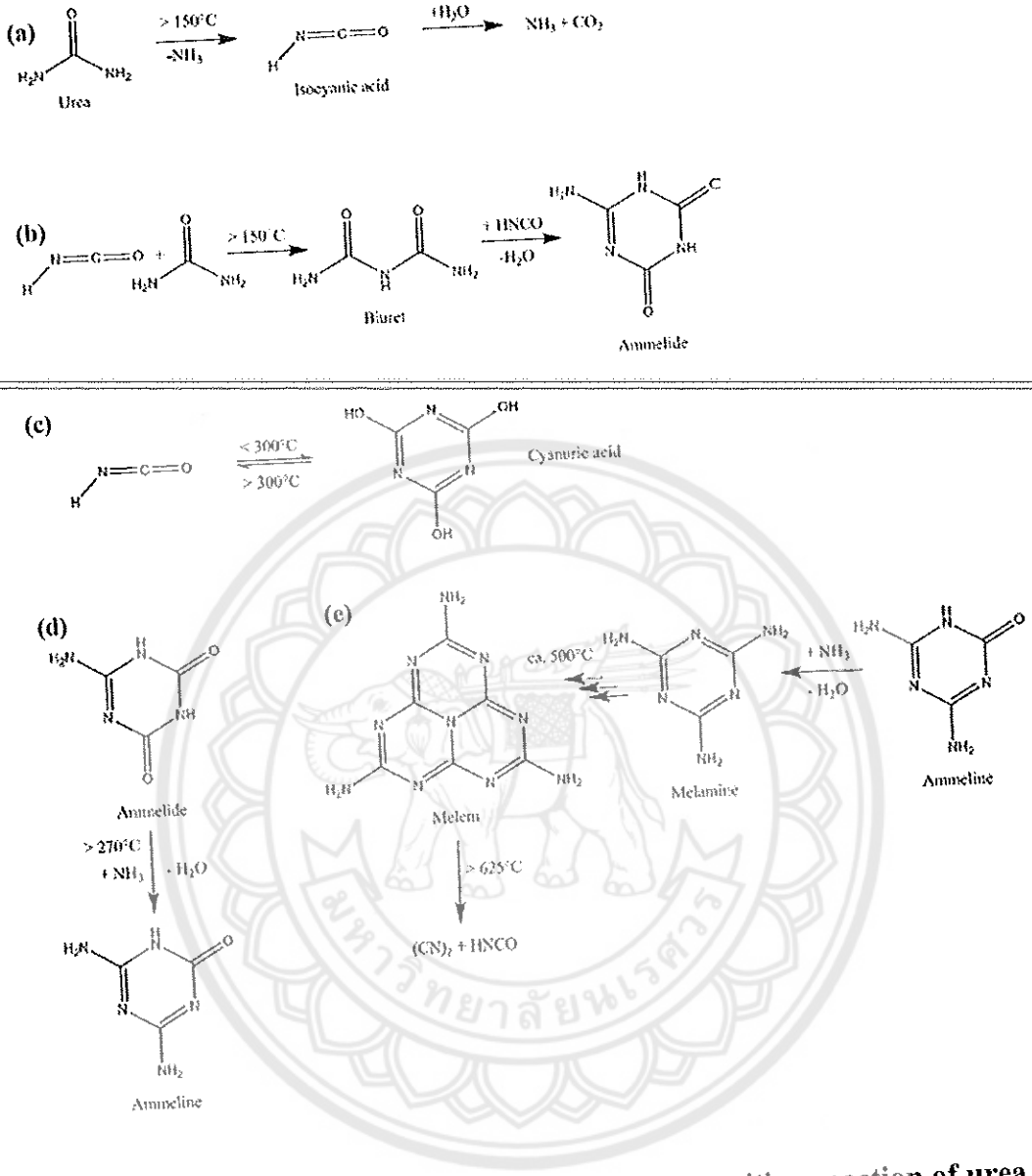

Figure 38 Schematic diagram of major decomposition reaction of urea [45]

3. Fuel content selection

The decomposition reactions of the organic compounds released high energy in multi-stages. Some research groups studied the synthesis of electroceramics with organic compound added, and expected the released energy from the decomposition reaction of fuel to be helpful in accelerating the chemical reaction of the raw materials [45-48]. Moreover, Hwang, et al. [20] suggested that the NH_3 released from the decomposition of organic compounds such as urea, glycine, alanine and citric acid could react with NO_x from the decomposed metal nitrate. The oxidation-reduction

reaction is shown in Eq.16. The energy released from this oxidation-reduction reaction accelerated the chemical reaction of raw materials.

$$4x\mathrm{NH_3} + 10\mathrm{NO}_x \rightarrow (5+2x)\mathrm{N_2} + 6x\mathrm{H_2O} + 2x\mathrm{O_2} \qquad \text{[Eq.16]}$$

There are two main energy releases during electroceramic synthesis in which the added raw materials consist of metal nitrate and organic compound. The first main energy is released from the decomposition reaction of fuel and the next one is released from the oxidation-reduction reaction between ammonia (decomposed from amine group of fuel) and NO_x (decomposed from metal nitrate of raw materials). This released energy helps to speed up the chemical reaction of the raw materials. However, it has been reported that an exothermic redox reaction (oxidation and reduction reaction taking place simultaneously) could be initiated only when the oxidizer and the fuel are mixed intimately in a fixed proportion. The basis of the combustion synthesis process is derived from the thermochemical concepts used in propellant chemistry [46, 47, 48, 49, 50, 51].

The ratio of the oxidizer and fuel for the redox mixture is calculated using the equivalence ratio (φ), defined as

$$\varphi = \frac{O}{F} \qquad \text{[Eq.17]}$$

Where (O) is the total oxidizing valence and (F) the total reducing valence of the elements present in the mixture [35]. According to propellant theory, the species M^{2+}, M^{3+}, M^{4+}, C and H are considered to be reducing with valencies of + 2, + 3,+ 4, + 4 and + 1 respectively. Oxygen is considered to be an oxidizing species with valence - 2 and nitrogen is considered to be valence neutral with a value of zero. Where the φ value is equal to unity (stoichiometric), the released energy reaches its maximum [46]. A mixture is fuel rich if $\varphi < 1$, fuel lean if $\varphi > 1$ [46].

Chavan, et al. [49] investigated the effects of oxidant-to-fuel ratio on the properties of Y_2O_3 synthesizing. The raw materials of $Y(NO_3)_3 \cdot 6H_2O$ and glycine (selected fuel) were mixed by the molar concentration in which the oxidant (yttrium nitrate) was kept constant at unity and the fuel concentration was varied. The elemental stoichiometric coefficient φ which is the ratio between the total valencies

of fuel (glycine; NH_2CH_2COOH) and that of the oxidizer (yttrium nitrate), can be calculated as shown below

$$\varphi = \frac{0_{(N)} + 2\times 1_{(H)} + 4_{(C)} + 2\times 1_{(H)} + 4_{(C)} - 2_{(O)} - 2_{(O)} + 1_{(H)}}{3_{(Y)} + 3\times 0_{(N)} + 9\times -2_{(O)}} \qquad \text{[Eq.18]}$$

In the present system, to satisfy this stoichiometric ratio the yttrium nitrate (oxidizing valency = 15−) to glycine (reducing valency = 9+) molar ratio was found to be 1:1.66. Previously the properties of powders had been studied by varying the molar ratios on either side of this ratio, i.e., fuel-lean compositions as 1:0.5, 1:1.0 and fuel rich i.e., 1:2.0, 1:2.5, 1:3.

Table 4 shows some properties of prepared powders with various oxidants to fuel ratio. The smallest crystallite size (8 nm) and the highest surface area (165 m^2/gm) were observed for the powder with a lean fuel condition (1:1.0). The powder with a stoichiometric composition had the largest crystallite size (30 nm) and the lowest surface area (57 m^2/gm). Thus the product with the best powder properties was the one from the lean fuel precursor, with an oxidant-to-fuel ratio of 1:1.0. These results could be attributed to two competing effects. The first one is the enthalpy of the reaction and the next is the subsequent flame temperatures associated with it and the number of moles of gaseous product evolved during combustion.

For the stoichiometric composition (1:1.66), which is a composition corresponding to the principle of propellant chemistry, the highest flame temperature observed (1440 °C) lead to large crystallites and a low surface area. Moreover, high temperature affects the prepared powders exhibited local partial sintering particle characteristics.

Increasing to a rich fuel composition (1:2.0, 1:2.5 and 1:3.0) decreased the flame temperature and there was no flame in the 1:3.0 composition. This was probably due to the lack of sufficient oxidant required for the complete combustion of the excess fuel. Moreover, increasing the fuel ratio caused the number of moles of gases released to also increase. These liberated gases dissipated the heat of combustion and limited the temperature rising, thus reducing the possibility of premature local partial sintering among the primary particles [49].

Table 9 Comparison of powder properties with different oxidant-to-fuel ratio [49]

Powders	O/F	Flame temperature (°C)	No. of moles of gases as per equation	Crystalline size (nm)	Surface area (m^2/g)	Sintered density (%)
a	1:0.5	No flame	11.88	12	44	-
b	1:1.0	No flame	13.00	8	165	97
c	1:1.66	1440	15.42	30	57	92
d	1:2.0	1200	17.50	25	147	94
e	1:2.5	1050	20.00	9	114	96
f	1:3.0	No flame	22.50	9	90	94

CHAPTER IV

THE EFFECTS OF FIRING TEMPERATURES ON PHASE FORMATION, MICROSTRUCTURE AND DIELECTRIC PROPERTIES OF $Bi_{0.5}(Na_{0.74}K_{0.16}Li_{0.10})_{0.5}TiO_3$ CERAMICS SYNTHESIZED VIA THE COMBUSTION ROUTE

Results and discussion

Figure 39 shows the XRD patterns of the BNKLT1610 powders calcined at different temperatures from 600 to 900 °C. At a low calcination temperature (600 °C), the diffraction peaks can be indexed as the rhombohedral perovskite phase for BNKLT1610. This corresponded to the thermal analyzed by literature [14], which indicated that the BNT perovskite crystal can be formed above 500 °C. However, a small amount of the secondary phase of $M_2Ti_6O_{13}$ as described by Naderer, et al. [14] was detected. The formation of the secondary phase was caused by the volatilization of K_2O with high lead vacancies concentration as shown in Eq.19.

$$0.25Bi_2O_3 + 0.1875Na_2CO_3 + 0.04K_2CO_3 + 0.025Li_2CO_3 + TiO_2 \rightarrow Bi_{0.5}Na_{0.375}K_{0.08-x}Li_{0.05}V'_{(K)x}TiO_{3-(x/2)}V_{O(x/2)}\bullet\bullet + \frac{x}{2}K_2O + 0.25CO_2 \quad \text{[Eq.19]}$$

The evaporation of K_2O caused a shift in the A/B ratio of cation in composition. To reduces the number of vacancies and reduces the deviation of the A/B ratio, the secondary phase of $M_2Ti_6O_{13}$ was formed from starting materials as shown in Eq.20 where M refers to Na and/or Li and/or K [14].

$$M_2CO_3 + 6TiO_2 \rightarrow M_2Ti_6O_{13} + CO_2 \quad \text{[Eq.20]}$$

By increasing the calcination temperature, the secondary phase was decreased and completely eliminated when the calcination temperature reached 750 °C. The calcining condition of 750 °C for 2 h, which produced pure the BNKLT1610 perovskite phase in this work was lower than that of the solid state reaction technique by 100 °C for 1 h [12]. This can be attributed to the energy released from the decomposition reaction of fuel which accelerated the chemical reaction of the raw materials [23, 24].The percentage of the perovskite phase was determined by

measuring the major XRD peak intensities which were calculated and are listed in Table 10.

To determine the lattice parameter a of the rhombohedral structure (Table 10), the BNT crystal structure was assumed as a hexagonal structure and the lattice parameters a and c were calculated. Then, the a and c lattice parameters were transformed to a lattice parameter a of rhombohedral structure using the following equation [80];

$$a_R = \frac{1}{3}\sqrt{3(a_H)^2 + c_H^2} \qquad \text{[Eq.21]}$$

Where a_R is the lattice parameter of rhombohedral structure, a_H and c_H are the lattice parameters a and c of a hexagonal structure, respectively. The variation of lattice parameter a evinced the differences diffusion of cations into sub-lattices.

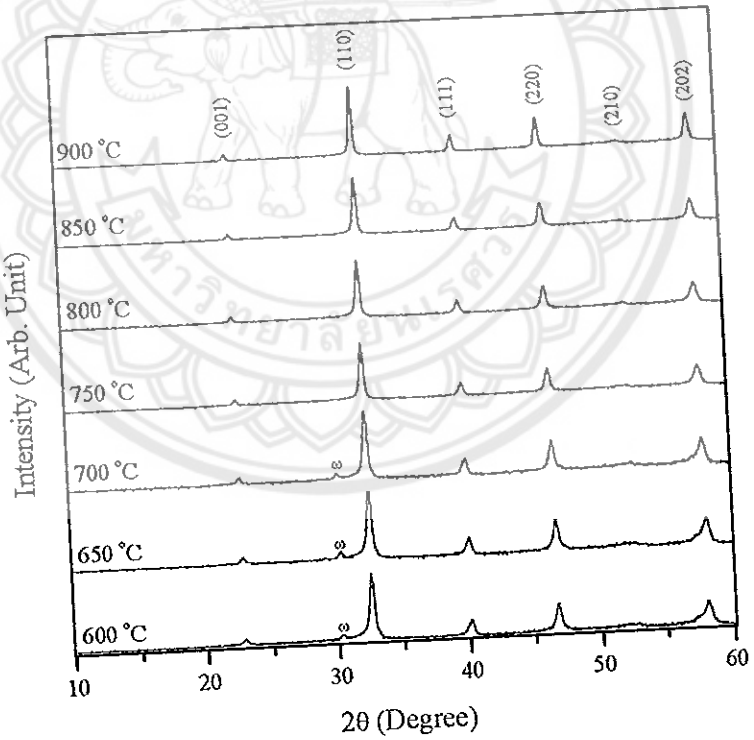

Figure 39 XRD patterns of BNKLT1610 powders calcined at different temperatures: (ω) $(K,Na,Li)_2Ti_6O_{13}$

The SEM photographs of BNKLT1610 powders calcined from 600 to 900 °C for 2 h are shown in Figure 40. The calcined powders consisted of fine particles, spherical shape and with an agglomerated form. Increasing the calcination temperature brought about a slight variation of particle size in the range of 110-360 nm as listed in Table 10. To obtain more particular characterizations, the TEM observation was investigated (Figure 41). When powders were calcined at a low temperature (Figure 41(a)), a dark zone appeared which indicated that electrons could not transmit through the multilayer of the sample. This demonstrated that a high agglomeration effect was induced. Increasing the calcination temperature up to 750 °C caused the agglomerated particles to be broken into fine individual particles (Figure 41(b)). The individual particles exhibited their particle size in the range of 100-200 nm, which is consistent with the SEM result. The individual particle shape was changed from a spherical to a cube shape when the calcination temperature was increased to 850 °C (Figure 41(c)). Moreover, many fine particles with a particle size lower than 100 nm were exhibited. This indicated that the combustion technique is an effective route to produce BNKLT1610 nanopowders.

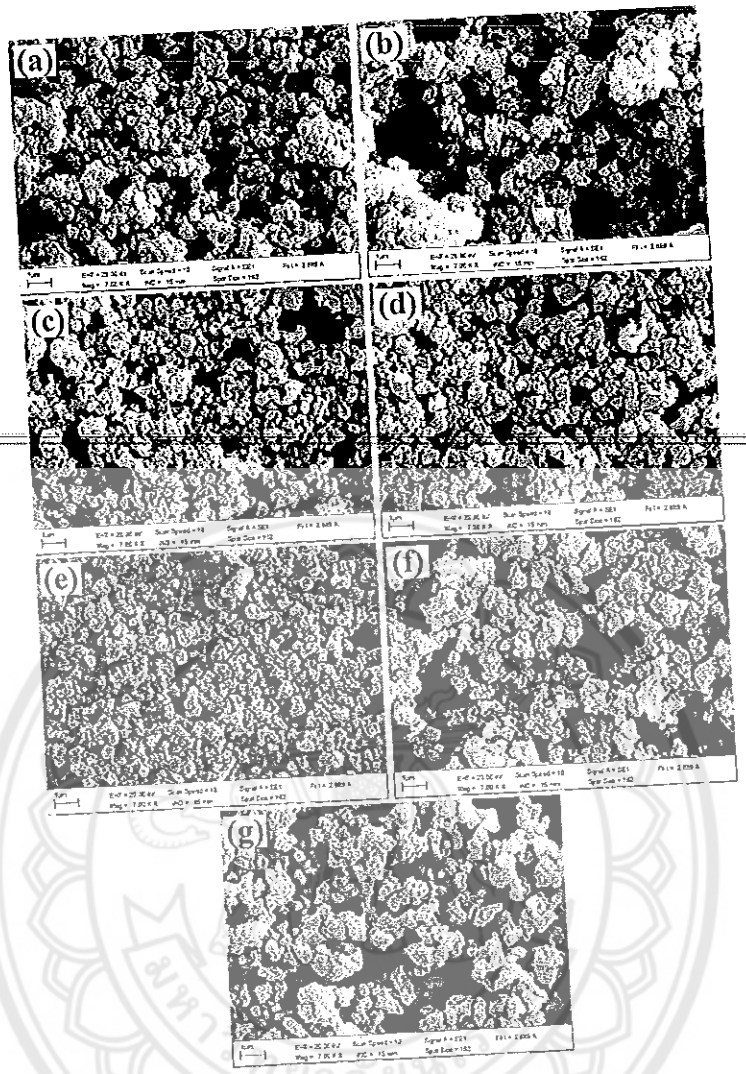

Figure 40 SEM photographs of BNKLT1610 powders calcined at; (a) 600 °C, (b) 650 °C, (c) 700 °C, (d) 750 °C, (e) 800 °C, (f) 850 °C and (g) 900 °C

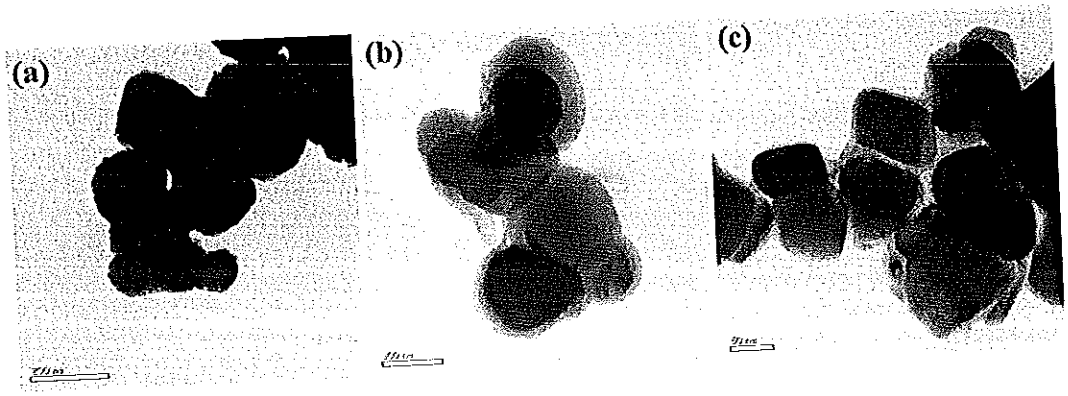

Figure 41 TEM micrographs of BNKLT1610 powders; (a) calcined at 650 °C, (b) calcined at 750 °C and (c) calcined at 850 °C

Table 10 Percent perovskite phase, lattice parameter *a* and average particle size of BNKLT1610 powders

Calcination temperature (°C)	% perovskite	Lattice parameter *a* (Å)	Average particle size (nm)
600	92.3	3.433	110
650	92.1	3.430	130
700	92.2	3.429	170
750	100	3.435	210
800	100	3.432	230
850	100	3.433	300
900	100	3.444	360

The powders calcined at 750 °C for 2 h were selected to fabricate the pellets and were sintered between 950 to 1,150 °C for 2 h. Figure 42(a) shows the XRD patterns of BNKLT1610 ceramics at various sintering temperatures. The pure perovskite phase was exhibited in ceramics sintered at 950 °C. By increasing sintering temperature up to 1,000 °C, the secondary phase of $M_2Ti_6O_{13}$ was repeatedly exhibited. The percentage of the perovskite phase was calculated and is listed in Table 11. Naderer, et al. [14] studied the secondary phase formation of $Bi_{0.5}Na_{0.375}K_{0.125}TiO_3$

ceramics. The results indicated that the ceramics initially decomposed at 990 °C and the secondary phase was formed at a temperature higher than 1,050 °C due to Bi_2O_3 and/or M_2O evaporating from the system. The formation of $M_2Ti_6O_{13}$ secondary phase at a high sintering temperature is described in Eq. 30.

$$16Bi_{0.5}M_{0.5}TiO_3 \rightarrow M_2Ti_6O_{13} + 10Bi_{0.5}M_{0.5}TiO_3 + \frac{3}{2}Bi_2O_3 + \frac{1}{2}M_2O \quad \text{[Eq. 30]}$$

The M-type could not be identified in this study. It is possible that M could be K and/or Li and/or Na. However, the secondary phase disappeared in the sample sintered at 1,150 °C. It is possible that it was volatized due to high firing temperature. This result is consistent with the literature which reports that the secondary phase in BKT decomposed at 1,120 °C [81].

The crystal structure of BNKLT1610 was investigated through XRD patterns which measured from 38 to 50° at a very low scanning rate (step size 0.00116°, time/θ 7.42 s, scan speed 0.05152 °/s) as is shown in Figure 42(b). Normally, BNT exhibits a rhombohedral structure (this is characterized by (003)/(021) peaks splitting at 2θ of 40° and a single peak of (202) at 2θ of 46.5°) whereas BKT exhibits tetragonal structure (which is a single peak of (111) at 2θ of 40° and splitting of (002)/(200) peaks at 2θ of 46.5°). Lu *et al.* [12] demonstrated that BNKLT1610 shows the coexistence of rhombohedral and tetragonal phases because its diffraction patterns showed splitting of (003)/(021) peaks at 2θ of 40° and splitting of (002)/(200) peaks at 2θ of 46.5° [12]. In this study, the BNKLT1610 ceramics sintered at 950 °C showed a slight splitting of (003)/(021) peaks at 2θ of 40° and an asymmetry peak of (200) at 2θ of 46.5°. So, this sample exhibited the mixed phases of rhombohedral-teragonal with the rhombohedral higher influenced on the crystal structure than the tetragonal phase. An increase of sintering temperature influenced the splitting of (003)/(021) peaks which decreased at 2θ of 40° while increasing the splitting of (200)/(002) peaks at 2θ of 46.5°. This indicated that the relative amounts of the tetragonal phases were increased. The splitting of diffraction peaks two positions 2θ of 40° and 46.5° was clearly observed in the sample sintered at 1,050 and 1,100 °C. This result indicated that the samples show the coexistence of rhombohedral and tetragonal phases. Moreover, increasing the sintering temperature to 1,150 °C caused the splitting of diffraction peaks at 2θ of 40° to decrease. This can be infers that the crystal structure

was slightly transformed to a tetragonal phase. The lattice parameter *a* of the sintered ceramics were calculated and are listed in Table 11.

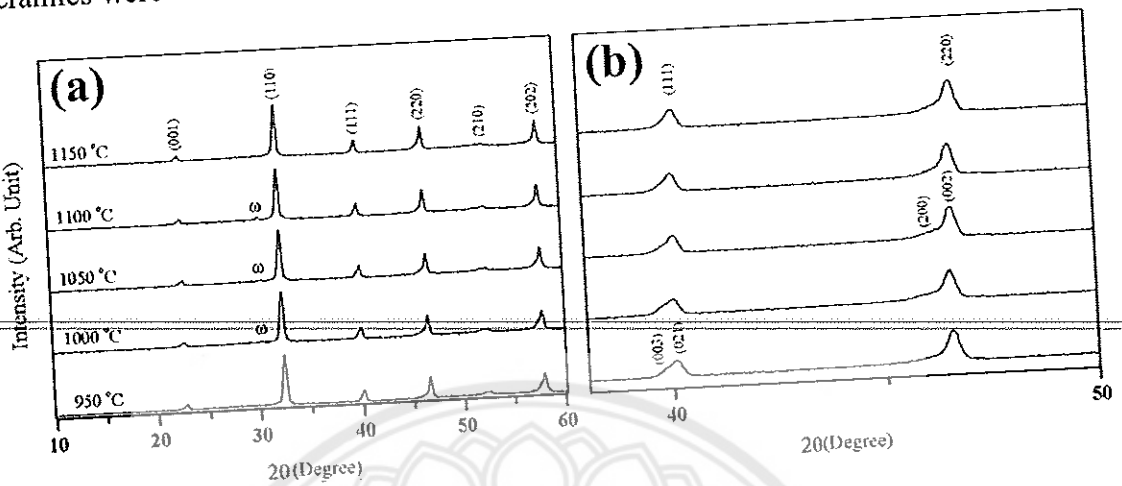

Figure 42 XRD patterns of BNKLT1610 ceramics sintered at various temperatures: (ω) $(K,Na,Li)_2Ti_6O_{13}$

Strong differences in the microstructure of the BNKLT1610 ceramics prepared at different sintering temperatures are seen in the SEM photographs in Figure 43. In the case of a low sintering temperature, the ceramics exhibited small grains with an irregular shape which represents the initial state of sintering (Figure 43(a)-(b)). Some of the melted plate was spread on the surface of the sample due to the evaporation of materials in the sintering process. By increasing the sintering temperature up to 1,050 °C (Figure 43(c)), the grain growth became increasingly active and the grain exhibited a quasi-cubic shape. However, the microstructure of the sintered ceramics showed a broad grain size distribution and many small grains exhibited initial grain growth characteristics. A narrow grain size distribution with clear grain boundaries, which is a feature of the grain growth process being nearly completed, is exhibited in the sample sintered at 1,100 °C for 2 h (Figure 43(d)). In addition, it should be noted that the surface micrograph of ceramics sintered at 1,150 °C shows evidence of melting grain, as can be seen in Figure 43(d). The variation of average grain size with increasing sintering temperatures was calculated and is listed in Table 11.

Figure 44 shows the SEM microstructures of the fracture surfaces of samples sintered with differences temperatures. Low sintering temperature brought about an

inadequate energy supply to the sample. Thus, the grains were weakened and transgranular fractures were exhibited (Figure 44(a) and (b)). By increasing the sintering temperature up to 1,050 °C, many intergranular fractures were observed as is shown in Figure 44(c). This indicates that the grains are sturdier than the grain boundaries. The intergranular fractures were distinctly observed when the sintering temperature was increased to 1,100 °C (Figure 44(d)). However, increase of sintered temperature to 1,150 °C caused the grain boundaries to be destroyed due to excessive heat (Figure 44(e)).

The measured density with a variation in sintering temperatures is listed in Table 11. The density of the ceramics was increased when sintering temperatures increased and reached its highest density at 1,100 °C with the value of 5.73 g/cm^3. Thereafter, the density decreased when the sintering temperature was increased to 1,150 °C. The reduction of density at high sintering temperature was caused by vitalization of the materials which induced high porosity in the sample. The density results corresponded with microstructure investigation. The highest density value of 5.73 g/cm^3 is higher than the density of 18 mol% K doped BNT ceramics (5.66 g/cm^3) [70] and slightly lower than the maximum density of K and Li doped BNT (5.76 g/cm^3) [82].

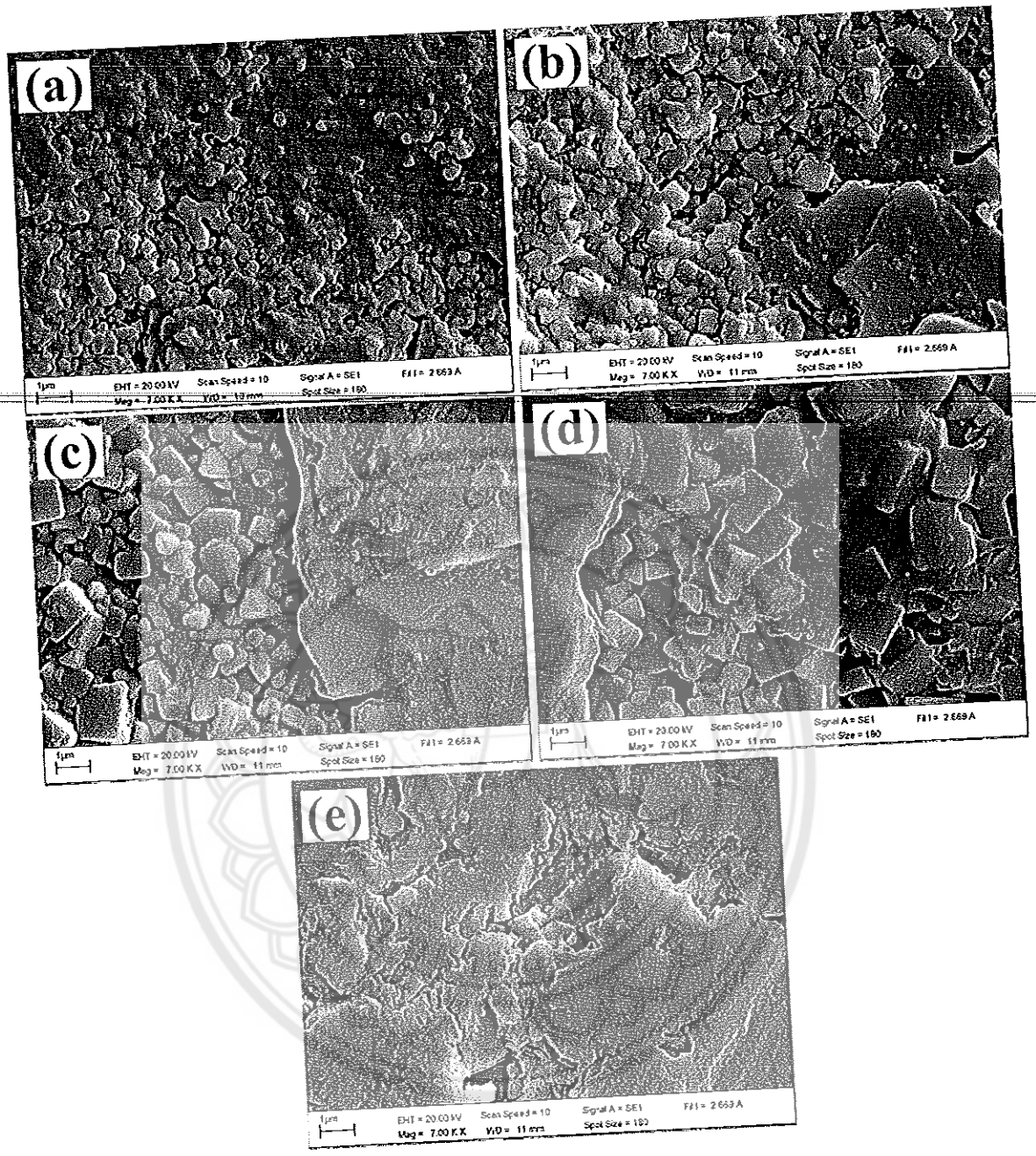

Figure 43 SEM photographs of surface BNKLT1610 ceramics sintered at; (a) 950 °C, (b) 1,000 °C, (c) 1,050 °C, (d) 1,100 °C and (e) 1,150 °C

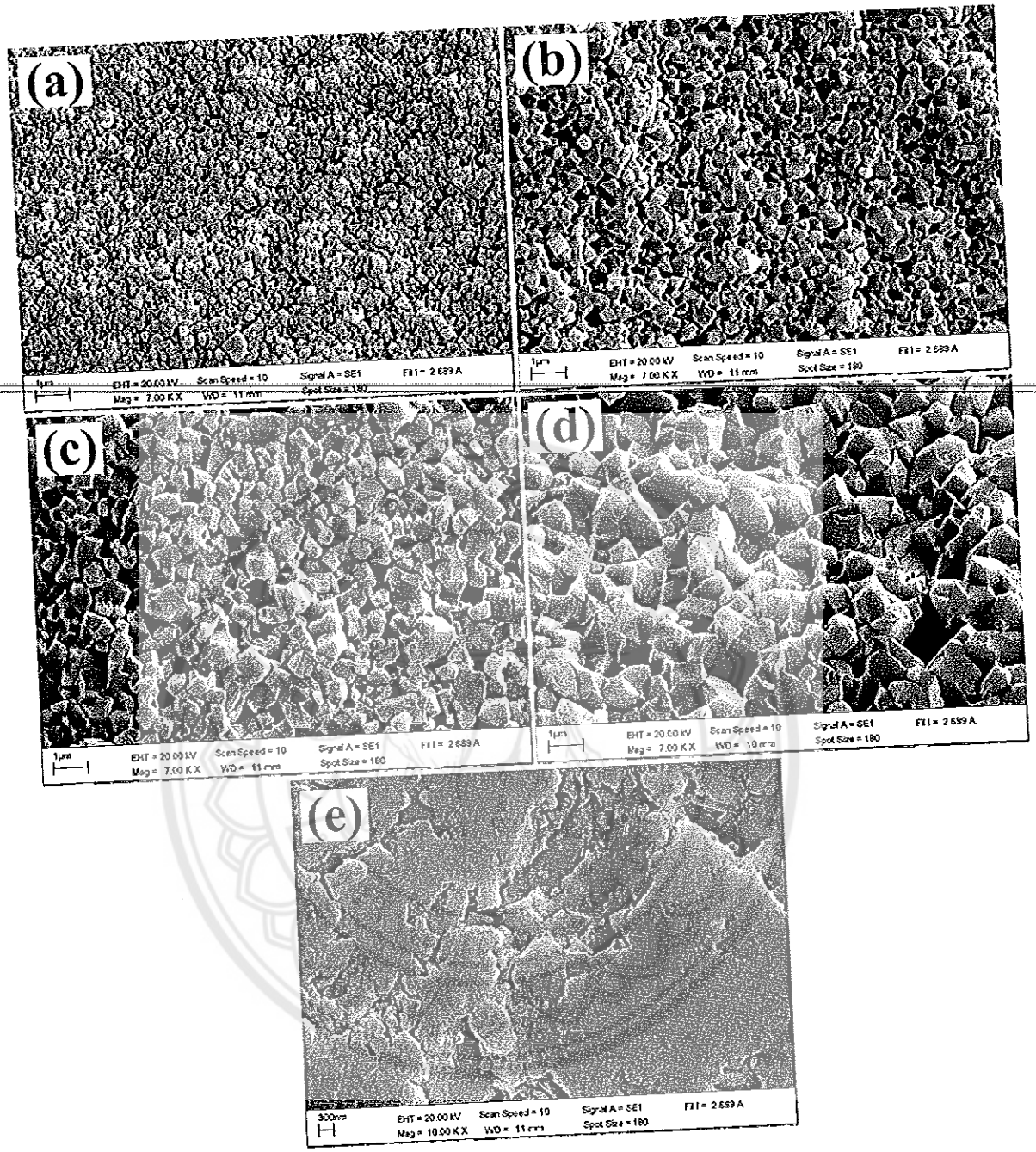

Figure 44 SEM photographs of fracture BNKLT1610 ceramics sintered at; (a) 950 °C, (b) 1,000 °C, (c) 1,050 °C, (d) 1,100 °C and (e) 1,150 °C

Table 11 Percent perovskite phase, lattice parameter *a*, average grain size and density of BNKLT1610 ceramics

Sintering temperature (°C)	Percent perovskite (%)	Lattice parameter *a* (Å)	Average grain size (nm)	Density (g/cm^3)
950	100	3.438	290	5.19
1,000	99.5	3.438	430	5.46
1,050	98.8	3.435	870	5.61
1,100	97.4	3.432	1,710	5.73
1,150	100	3.426	-	4.97

Figure 45 shows the temperature dependence of the dielectric constant and the tanδ of the BNKLT1610 ceramics sintered at various temperatures and measured at 1 kHz. Normally, the dielectric curve of BNT shows two distinct dielectric constant peaks at 125 and 320 °C. The first peak infers the phase transition from rhombohedral ferroelectric to a tetragonal anti-ferroelctric phase. The temperature at this phase transition point is called depolarization temperature (T_d). The next dielectric peak, which the dielectric constant shows its highest value, was observed at ~320 °C. This dielectric peak may be caused by the anti-ferroelctric phase transforming to the paraelctric phase and the temperature at this point is abbreviate as the maximum dielectric temperature (T_m). For this study, the BNKLT1610 ceramics sintered at 950 °C showed only one dielectric peak at temperature ~200 °C (T_d). The dielectric peak at T_m could not be observed. By increasing the sintering temperature to 1,000 °C, the dielectric peak at T_d distinctly appears. Moreover, a faint dielectric peak at a higher temperature (~320 °C) was observed. This is possibly the dielectric peak at T_m. The altitude of the dielectric peak at T_m is lower than the T_d altitude. The dielectric peak at T_m was more clearly observed when the sintering temperature increase to 1,050 °C. Increasing sintering temperature to 1,100 °C caused the dielectric peak at T_m to be distinctly exhibited and the maximum dielectric constant is observed at this point. For the sample sintered at 1,150 °C, the two dielectric peaks were clearly separated. The characteristics and position of the two dielectric peaks corresponded with the dielectric

curve of BNT ceramics reported by the literatures [68, 75]. The phase transition temperature of T_d and T_m was clearly specified from the dielectric loss curve. Table 12 summarizes the phase transition temperature of T_d and T_m, including the values of the dielectric constant of each peak, which were observed from the dielectric loss curve. Excluding the sample sintered at 950 °C, an increase of sintering temperature caused T_d to decrease and to dramatically decrease for samples sintered at high temperatures. In the case of T_m, it could not be observed from the sample sintered at 950 °C. An increase of sintering temperature caused T_m to experience a disorderly shift in the other samples. The dielectric constant at T_d (ε_d) and at T_m (ε_m) for various sintering temperatures are graphically presented in Figure 46. It can be seen that the value of ε_d is slightly higher than ε_m for sample sintered at 1,000 °C. The interval between ε_d and ε_m decreased when the sintering temperature increased to 1,050 °C. Thereafter, an increase of sintering temperature to 1,100 °C caused the value of ε_m to be slightly higher than ε_d. This interval increased when increasing the sintering temperature to 1,150 °C. The differences between ε_d and ε_m were calculated and are listed in Table 12. Park, et al. [83] suggested that the altitude of the dielectric constant peak at Curie temperatures and lower temperature are correlated with the grain core and grain shell, respectively, which is exhibited in the core-shell structure materials. The core-shell structure can be formed in ferroelectric ceramics such as BT and BNT which some cation additives [83]. The core-shell structure consists of relatively pure composition grain cores embedded in and surrounded by a second impurity phase grain shell [84]. In this study, the dielectric constant peak at T_m was indistinctly observed while the dielectric constant peak at T_d dominated for the sample sintered at a low temperature (Figure 45(a)). This suggests that the core-shell structure was formed in the system and the influence of the grain shell is higher than the grain core so the dielectric constant peak at T_d is more dominate than at T_m. By increasing sintering temperature, the dielectric constant peak at T_m seems more visible (Figure 45(b)-(c)). This suggests that the grain core was enlarger and grain shell was thinner. The sample sintered at 1,100 °C shows a dielectric constant peak at T_m more easily observed than the dielectric peak at T_d (Figure 45(d)). This indicated that the grain core is more highly influenced by the dielectric constant than the grain shell. This behavior was more distinctly exhibited in the sample sintered at 1,150 °C (Figure 45(e)). The enlarging of

the grain core and the thinning of the grain shell due to higher sintering temperature was probably due to with the higher evaporation of $Bi_{0.5}M_{0.5}TiO_3$ in Eq. 30.

The value of the dielectric constant and dielectric loss at room temperature (ε_r and tanδ) are listed in Table 11 and the variable of ε_r due to differences of sintering temperatures has been plotted as shown in Figure 46. By increasing sintering temperature from 950 to 1,000 °C, the ε_r tended to increase due to higher grain growth and densification. Thereafter, an increase of sintering temperature induced ε_r to decrease though the average grain size and density were enhanced. This can be attributed to the secondary phase affects. The value of ε_r was enhanced again when the sintering temperature was increased up to 1,150 °C. This was caused by the secondary phase being eliminated from the system. However, the low density due to the grains and grain boundaries being melted limited the ε_r value. Lu, et al. [12] reported the ε_r value of BNT with 10 mol% Li doped BNT, 16 mol% K doped BNT and BNKLT1610 ceramics prepared via the solid-state reaction method are 420, 480, 1,020 and 1,080, respectively. Nevertheless, these values are lower than the maximum ε_r of 1,210 obtained from this study. This demonstrates the potential for Li and K being substituted in BNT and the efficiency of the combustion technique for preparing BNKLT1610 ceramics.

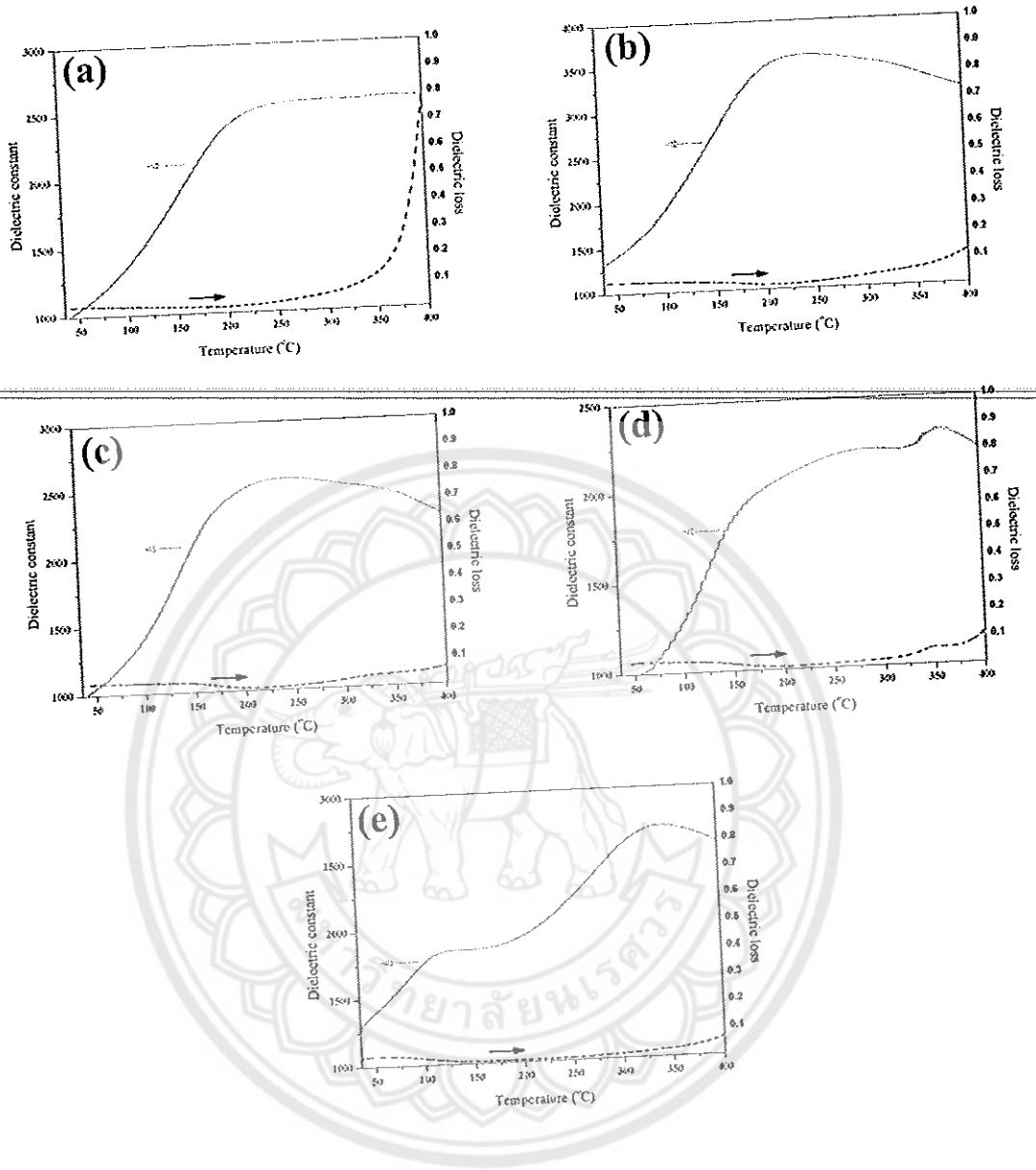

Figure 45 Temperature dependences of dielectric constant and dielectric loss of the BNKLT1610 ceramics sintered at; (a) 950 °C, (b) 1,000 °C, (c) 1,050 °C, (d) 1,100 °C and (e) 1,150 °C

Table 12 The T_d, T_m, ε_d, ε_m, $\Delta\varepsilon_{md}$, ε_r and tanδ of BNKLT1610 ceramics

Sintering temperature (°C)	T_d (°C)	T_m (°C)	ε_d	ε_m	$\Delta\varepsilon_{md}$	ε_r	tanδ
950	180	-	2,550	-	-	910	0.033
1,000	215	323	3,580	3,495	-85	1,210	0.036
1,050	204	330	2,530	2,490	-40	900	0.036
1,100	184	348	2,000	2,280	280	880	0.039
1,150	140	334	1,860	2,710	850	1,190	0.032

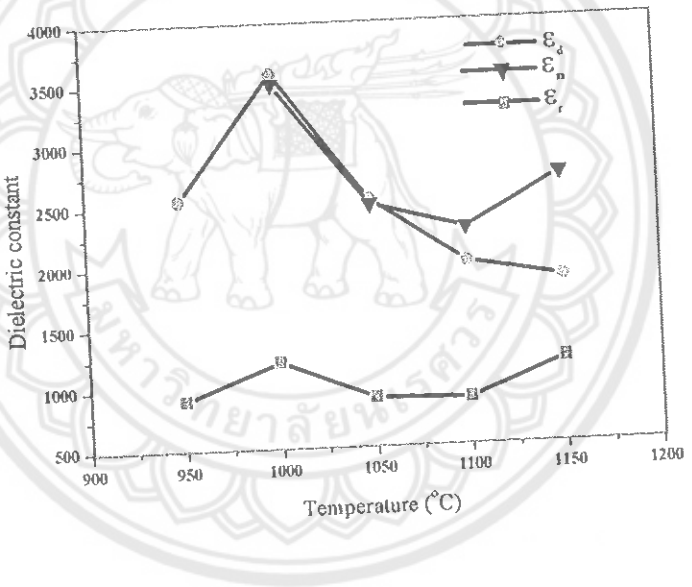

Figure 46 ε_d, ε_m and ε_r as function of sintering temperature of BNKLT1610 ceramics

CHARPTER V

CONCLUSION

Lead-free BNKLT1610 ceramics were successfully synthesized using the combustion technique. The effects of firing temperatures on phase formation, microstructure and dielectric properties were observed. The XRD revealed pure BNKLT1610 was produced when the calcination temperature was higher than 700 °C. Low calcining temperatures caused the volatilization of K_2O and a secondary phase was formed. After being sintered between 950-1,150 °C, pure BNKLT1610 ceramics were obtained from the samples sintered at 950 °C and 1,150 °C. For the samples sintered at other temperatures, the secondary phase was repeatedly formed. An increase of sintering temperature from 950 °C to 1,100 °C enhanced grain size and densification while the sample sintered at 1,150 °C exhibited inferior morphology and a low density due to the evaporation of materials. The dielectric properties were highly influenced from the formation of the secondary phase and densification. Moreover, the grain core and grain shell formation highly influenced the variation of the dielectric constant values at phase transition points. The sample sintered at 1,000 °C shows the highest dielectric constant at room temperature (ε_r) and maximum dielectric constant (ε_m) with the values of 1,210 and 3,495, respectively. The sample sintered at 1,100 °C showed the highest densification but the formation of the secondary phase limited their dielectric properties. The highest value of ε_r in this study is significantly higher than those of other reports. This suggests the combustion technique effectively produces high quality BNKLT1610 ceramics.

REFERENCES

REFERENCES

[1] Jaita, P., Watcharapasorn, A. and Jiansirisomboon, S. (2011). Effects BNT compound incorporated on structure and electrical properties of PZT ceramic. **Current Applied Physics**, 11, S77-S81.

[2] Lu, W., Wang, Y., Fan, G., Wang, X. and Liang, F. (2011). The structural and electric properties of Li- and K-substituted $Bi_{0.5}Na_{0.5}TiO_3$ ferroelectric ceramics. **Journal of Alloys and Compounds**, 509, 2738-2744.

[3] Zuo, R., Su, S., Wu, Y., Fu, J., Wang, M. and Li, L. (2008). Influence of A-site nonstoichiometry on sintering, microstructure and electrical properties of $(Bi_{0.5}Na_{0.5})TiO_3$ ceramics. **Materials Chemistry and Physics**, 110, 311-315.

[4] Choy, S. H. and Chan, H. L. W. (2011). Nonlinear behavior of BNT-based lead-free piezoceramics under various ac fields. **Current Applied Physics**, 11, 869-877.

[5] Yang, Z., Liu, B., Wei, L. and Hou, Y. (2008). Structure and electrical properties of $(1-x)Bi_{0.5}Na_{0.5}TiO_3$–$xBi_{0.5}K_{0.5}TiO_3$ ceramics near morphotropic phase boundary. **Materials Research Bulletin**, 43, 81-89.

[6] Zuo, R., Su, S., Wu, Y., Fu, J., Wang, M. and Li, L. (2008). Influence of A-site nonstoichiometry on sintering, microstructure and electrical properties of $(Bi_{0.5}Na_{0.5})TiO_3$ ceramics. **Materials Chemistry and Physics**, 110, 311-315.

[7] Zhang, Y., Zheng, X. and Zhang, T. (2011). Characterization and humidity sensing properties of $Bi_{0.5}Na_{0.5}TiO_3$–$Bi_{0.5}K_{0.5}TiO_3$ powder synthesized by metal-organic decomposition. **Sensors and Actuators B: Chemical**, 156, 887-892.

[8] Liao, Y., Xiao, D., Lin, D., Zhu, J., Yu, P., Wu, L., et al. (2007). Synthesis and properties of $Bi0.5(Na_{1-x-y}K_xAg_y)_{0.5}TiO_3$ lead-free piezoelectric ceramics. **Ceramics International**, 33, 1445-1448.

[9] Naderer, M., Schütz, D., Kainz, T., Reichmann, K. and Mittermayr, F. (2012). The formation of secondary phases in $Bi_{0.5}Na_{0.375}K_{0.125}TiO_3$ ceramics. **Journal of the European Ceramic Society**, 32(10), 2399-2404.

[10] Lin, D., Kwok, K. W. and Chan, H. L. W. (2008). Structure and electrical properties of $Bi_{0.5}Na_{0.5}TiO_3$–$BaTiO_3$–$Bi_{0.5}Li_{0.5}TiO_3$ lead-free piezoelectric ceramics. **Solid State Ionics**, 178, 1930-1937.

[11] Naderer, M., Schütz, D., Kainz, T., Reichmann, K. and Mittermayr, F. (2012). The formation of secondary phases in $Bi_{0.5}Na_{0.375}K_{0.125}TiO_3$ ceramics. **Journal of the European Ceramic Society**, 32, 2399-2404.

[12] Choy, S. H. and Chan, H. L. W. (2011). Nonlinear behavior of BNT-based lead-free piezoceramics under various ac fields. **Current Applied Physics**, 11, 869-877.

[13] Hou, Y., Hou, L., Zhu, M., Wang, H. and Yan, H. (2007). Sol–gel synthesis of lead-free $(K_{0.5}Bi_{0.5})_{0.4}Ba_{0.6}TiO_3$ nanorods. **Materials Letters**, 61, 3371-3373.

[14] Liu, Y., Lu, Y. and Dai, S. (2009). Hydrothermal synthesis of monosized $Bi_{0.5}Na_{0.5}TiO_3$ spherical particles under low alkaline solution concentration. **Journal of Alloys and Compounds**, 484, 801-805.

[15] Chen, W., Kume, S. and Watari, K. (2005). Molten salt synthesis of $0.94(Na_{1/2}Bi_{1/2})TiO_3$–$0.06BaTiO_3$ powder. **Materials Letters**, 59, 3238-3240.

[16] Hwang, C.-C., Wu, T.-Y., Wan, J. and Tsai, J.-S. (2004). Development of a novel combustion synthesis method for synthesizing of ceramic oxide powders. **Materials Science and Engineering: B**, 111, 49-56.

[17] Mangalaraja, R. V., Mouzon, J., Hedström, P., Kero, I., Ramam, K. V. S., Camurri, C. P., et al. (2008). Combustion synthesis of Y_2O_3 and Yb–Y_2O_3: Part I. Nanopowders and their characterization. **Journal of Materials Processing Technology**, 208, 415-422.

[18] Thongtha, A.and Bongkarn, T. (2009). Phase formation and microstructure of barium zirconate ceramics prepared using the combustion technique. **Ferroelectrics**, 383, 33-39.

[19] Panya, P. and Bongkarn, T. (2009). Fabrication of perovskite barium titanate ceramics using combustion route. **Ferroelectrics**, 383, 102–110.

[20] Moulson, A. J. and Herbert, J. M. (1992). **Electroceramics**. London: Chapman & Hall.

[21] Barsoum, M. W. (2003). **Fundamentals of ceramics**. London: McGraw-Hill.

[22] Haertling, G. H. (1999). Ferroelectric ceramics: history and technology. **J. Am. Ceram. Soc.**, 82, 797–818.

[23] Safari, A., Panda, R. K. and Janas, V. F. (1996). Lead-free materials. **Key Engineering Materials**, 122, 35-70.

[24] Loehman, R. E. (2010). **Characterization of ceramics**. New York: Taylor&Francis.

[25] Dixit, A., Majumder, S. B., Dobal, P. S., Katiyar, R. S. and Bhalla, A. S. (2004). Phase transition studies of sol–gel deposited barium zirconate titanate thin films. **Thin Solid Films**, 447–448, 284-288.

[26] Ciomaga, C.E., Calderone, R., Buscaglia, M.T., Viviani, M., Buscaglia, V., Mitoseriu, L., Stancu, A. and Nanni, P. (2006) Relaxor properties of $Ba(Zr,Ti)O_3$ ceramics. **J. Optoelectron. Adv. Mater**, 8, 944–948.

[27] Chen, H., Yang, C., Fu, C., Shi, J., Zhang, J. and Leng, W. (2008). Microstructure and dielectric properties of $BaZr_xTi_{1-x}O_3$ ceramics. **J. Mater. Sci.**, 19, 379–382.

[28] Reddy, S. B., Rao, K. P. and Rao, M. S. R. (2007). Nanocrystalline barium zirconate titanate synthesized at low temperature by an aqueous co-precipitation technique. **Scripta Materialia,** 57, 591-594.

[29] Kuang, S. J., Tang, X. G., Li, L. Y., Jiang, Y. P. and Liu, Q. X. (2009). Influence of Zr dopant on the dielectric properties and Curie temperatures of $Ba(Zr_xTi_{1-x})O_3$ $(0 \leq x \leq 0.12)$ ceramics. **Scripta Materialia,** 61, 68-71.

[30] Huang, H.H., Chiu, H.H.S., Wu, N.C. and Wang, M.C. (2008). Tetragonality and properties of $Ba(Zr_xTi_{1-x})O_3$ ceramics determined using the Rietveld method. **Metallurgical and Materials Transactions**, 39A, 3276–3284.

[31] Neirman, S. M. (1988). The Curie point temperature of Ba(ZrxTi1-x)O3solid solutions. **Journal of Materials Science**, 23, 3973-3980.

[32] Binhayeeniyi, N., Sukvisut, P., Thanachayanont, C. and Muensit, S. (2010). Physical and electromechanical properties of barium zirconium titanate synthesized at low-sintering temperature. **Materials Letters,** 64, 305-308

[33] Yu, Z., Ang, C., Guo, R. and Bhalla, A. S. (2007). Dielectric properties of $Ba(Zr_xTi_{1-x})O_3$solid solutions. **Materials Letters**, 61, 326-329.

[32] Hwang, C.-C., Wu, T.-Y., Wan, J. and Tsai, J.-S. (2004). Development of a novel combustion synthesis method for synthesizing of ceramic oxide powders. **Materials Science and Engineering: B**, 111, 49-56.

[33] Nanakorn, N., Jalupoom, P., Vaneesorn, N. and Thanaboonsombut, A. (2008). Dielectric and ferroelectric properties of $Ba(Zr_xTi_{1-x})O_3$ ceramics. **Ceramics International**, 34, 779-782.

[34] Pookmanee, P., Rujijanagul, G., Ananta, S., Heimann, R. B. and Phanichphant, S. (2004). Effect of sintering temperature on microstructure of hydrothermally prepared bismuth sodium titanate ceramics. **Journal of the European Ceramic Society**, 24(2), 517-520.

[35] Ji, W.-J., Chen, Y.-B., Zhang, S.-T., Yang, B., Zhao, X.-N. and Wang, Q.-J. (2012). Microstructure and electric properties of lead-free $0.8Bi_{1/2}Na_{1/2}TiO_3$–$0.2Bi_{1/2}K_{1/2}TiO_3$ ceramics. **Ceramics International**, 38, 1683-1686.

[36] Chou, C.-S., Wu, C.-Y., Yang, R.-Y. and Ho, C.-Y. (2012). Preparation and characterization of the bismuth sodium titanate ($Na_{0.5}Bi_{0.5}TiO_3$) ceramic doped with ZnO. **Advanced Powder Technology**, 23, 358-365.

[37] Hiruma, Y., Nagata, H. and Takenaka, T. (2009). Depolarization temperature and piezoelectric properties of $(Bi_{1/2}Na_{1/2})TiO_3$–$(Bi_{1/2}Li_{1/2})TiO_3$–$(Bi_{1/2}K_{1/2})TiO_3$ lead-free piezoelectric ceramics. **Ceramics International**, 35, 117-120.

[38] Pookmanee, P., Rujijanagul, G., Ananta, S., Heimann, R. B. and Phanichphant, S. (2004). Effect of sintering temperature on microstructure of hydrothermally prepared bismuth sodium titanate ceramics. **Journal of the European Ceramic Society**, 24(2), 517-520.

[39] Ji, W.-J., Chen, Y.-B., Zhang, S.-T., Yang, B., Zhao, X.-N. and Wang, Q.-J. (2012). Microstructure and electric properties of lead-free $0.8Bi_{1/2}Na_{1/2}TiO_3$–$0.2Bi_{1/2}K_{1/2}TiO_3$ ceramics. **Ceramics International**, 38, 1683-1686.

[40] Chou, C.-S., Wu, C.-Y., Yang, R.-Y. and Ho, C.-Y. (2012). Preparation and characterization of the bismuth sodium titanate ($Na_{0.5}Bi_{0.5}TiO_3$) ceramic doped with ZnO. **Advanced Powder Technology**, 23, 358-365.

[41] Hiruma, Y., Nagata, H. and Takenaka, T. (2009). Depolarization temperature and piezoelectric properties of $(Bi_{1/2}Na_{1/2})TiO_3$–$(Bi_{1/2}Li_{1/2})TiO_3$–$(Bi_{1/2}K_{1/2})TiO_3$ lead-free piezoelectric ceramics. **Ceramics International**, 35, 117-120.

[42] Yang, Z., Liu, B., Wei, L. and Hou, Y. (2008). Structure and electrical properties of $(1-x)Bi_{0.5}Na_{0.5}TiO_3$–$xBi_{0.5}K_{0.5}TiO_3$ ceramics near morphotropic phase boundary. **Materials Research Bulletin**, 43, 81-89.

[43] Chu, B.-J., Chen, D.-R., Li, G.-R. and Yin, Q.-R. (2002). Electrical properties of $Na_{1/2}Bi_{1/2}TiO_3$–$BaTiO_3$ ceramics. **Journal of the European Ceramic Society**, 22, 2115-2121.

[44] Peng, C., Li, J.-F. and Gong, W. (2005). Preparation and properties of $(Bi_{1/2}Na_{1/2})TiO_3$–$Ba(Ti,Zr)O_3$ lead-free piezoelectric ceramics. **Materials Letters**, 59, 1576-1580.

[45] Eichelbaum, M., Farrauto, R. J. and Castaldi, M. J. (2010). The impact of urea on the performance of metal exchanged zeolites for the selective catalytic reduction of NOx: Part I. Pyrolysis and hydrolysis of urea over zeolite catalysts. **Applied Catalysis B: Environmental**, 97, 90-97.

[46] Chaiyo, N., Muanghlua, R., Niemcharoen, S., Boonchom, B. and Vittayakorn, N. (2011). Solution combustion synthesis and characterization of lead-free piezoelectric sodium niobate ($NaNbO_3$) powders. **Journal of Alloys and Compounds**, 509, 2445-2449.

[47] Pampuch, R. (1999). Advanced HT ceramic materials via solid combustion. **Journal of the European Ceramic Society**, 19, 2395-2404.

[48] Fumo, D. A., Jurado, J., Segadães, A. M. and Frade, J. R. (1997). Combustion synthesis of iron-substituted strontium titanate perovskites. **Materials Research Bulletin**, 32, 1459-1470.

[49] Chavan, S. V., Pillai, K. T. and Tyagi, A. K. (2006). Combustion synthesis of nanocrystalline yttria: Tailoring of powder properties. **Materials Science and Engineering: B**, 132, 266-271.